

8-2021

Mixing Optimization With Inward Flow Configuration Contra-Rotating Impeller, Baffle-Free Tank

P. Satjaritanun

J. R. Regalbuto

J. A. Regalbuto

N. Tippayawong

Sirivatch Shimpalee

University of South Carolina, shimpale@cec.sc.edu

Follow this and additional works at: https://scholarcommons.sc.edu/eche_facpub



Part of the [Chemical Engineering Commons](#)

Publication Info

Published in *Alexandria Engineering Journal*, Volume 60, Issue 4, 2021, pages 3759-3779.

This Article is brought to you by the Chemical Engineering, Department of at Scholar Commons. It has been accepted for inclusion in Faculty Publications by an authorized administrator of Scholar Commons. For more information, please contact digres@mailbox.sc.edu.



Alexandria University
Alexandria Engineering Journal

www.elsevier.com/locate/aej
www.sciencedirect.com



Mixing optimization with inward flow configuration contra-rotating impeller, baffle-free tank



P. Satjaritanun^a, J.R. Regalbuto^a, J.A. Regalbuto^b, N. Tippayawong^{c,1},
S. Shimpalee^{a,c,*}

^a Department of Chemical Engineering, University of South Carolina, Columbia, SC, USA

^b Perfect Mixing LLC, Columbia, SC, USA

^c Department of Mechanical Engineering, Chiang Mai University, Thailand

Received 30 November 2020; revised 21 January 2021; accepted 22 February 2021

Available online 5 March 2021

KEYWORDS

Contra-rotating impellers;
Taguchi method;
Perfect mixing;
Lattice Boltzmann method;
Design optimization

Abstract In this study, pitched-blade, contra-rotating impeller, baffle-free tank with opposing inward flow is optimized using various designs of mixers derived from the Taguchi method. Mixing efficiency and torque are used to find the optimal design for the different specific gravities of solid particles employing in both experiments and CFD simulations. The analysis of signal-to-noise ratio shows that the impeller clearance and diameter are significant factors on the fluid flow and thus the mixing efficiency. In this study, 27 cases were studied to determine and report the optimal design parameters. A combination of CFD simulation with a strong design of experiment illustrates the ability to characterize and optimize the design parameters that affect mixing efficiency, showing promise as design guideline for the contra-rotating impeller. The best compromise between high mixing efficiency and low torque for pilot scale was found in the following configuration: a 300 mm diameter tank with liquid filled to a height of 300 mm; four pitched-blades rotating at 100 RPM with an impeller diameter of 150 mm; and a 125 mm impeller-impeller and impeller-bottom clearance.

© 2021 THE AUTHORS. Published by Elsevier BV on behalf of Faculty of Engineering, Alexandria University. This is an open access article under the CC BY-NC-ND license (<http://creativecommons.org/licenses/by-nc-nd/4.0/>).

1. Introduction

Slurries of agitated, suspended solid particles have been used to enhance the rate of mass transfer between solid particles and the liquid phase [1]. Contra-rotating impellers mix the contents in the mixing reactor without forming a vortex and do not require baffles in the tank [2], which minimizes torque and simplifies operation and maintenance. In solid suspension applications, the solid particles will swirl around at the bottom of the tank. A contra-rotating impeller configuration creates a

* Corresponding author at: Department of Chemical Engineering, University of South Carolina, Columbia, SC, USA.
E-mail addresses: nakorn.t@cmu.ac.th (N. Tippayawong), shimpalee@cec.sc.edu (S. Shimpalee).

¹ Co-corresponding author.

Peer review under responsibility of Faculty of Engineering, Alexandria University.

<https://doi.org/10.1016/j.aej.2021.02.045>

1110-0168 © 2021 THE AUTHORS. Published by Elsevier BV on behalf of Faculty of Engineering, Alexandria University.
This is an open access article under the CC BY-NC-ND license (<http://creativecommons.org/licenses/by-nc-nd/4.0/>).

Nomenclature

| | |
|--------------------|---|
| $\bar{a}_{D(p-p)}$ | acceleration of the particle due to the drag force |
| \bar{a}_{Extfp} | external acceleration force (e.g. gravity) |
| \bar{a}_{Extp} | external acceleration affecting only disperse phase |
| b | control level of Taguchi method |
| c | control factor of Taguchi method |
| C | impeller-bottom clearance |
| CoV | coefficient of variation |
| CV | distance between the upper impeller and the top of liquid surface |
| D | impeller diameter |
| \bar{e}_j | particle discrete set of velocities |
| eff | mixing efficiency |
| f_{act} | actual particle fraction |
| f_{ideal} | ideal particle fraction |
| f_j | particle distribution function in direction j |
| h | image of horizontal plane |
| H | liquid height |
| La | number of experimental runs |
| m | probability distribution function of the particle distribution function |
| \bar{n} | unit normal vector at the control volume surface |
| n | rotation speed |
| N_B | number of blades |
| N_{ideal} | total number of particles were fed into the liquid |
| N_P | power number |
| $N_{Taguchi}$ | minimum number of experiments |
| P | power required by the impeller |
| \vec{r} | radius vector of propeller |
| S | impeller-impeller clearance |
| S/N | signal-to-noise ratio |

| | |
|-------------|-----------------------------------|
| t | discrete times |
| Δt | constant time step |
| T | tank diameter |
| T_r | torque |
| \bar{u}_p | particle velocity |
| \bar{V} | fluid velocity |
| x | lattice node |
| ρ | density |
| v | image of vertical plane |
| μ | molecular viscosity of the fluid |
| Ω_j | collision operator |
| Re | Reynolds number |
| δ_h | deviation in the horizontal plane |
| δ_v | deviation in the vertical plane |
| s_k | deviation from ideal mixing |

Abbreviations

| | |
|-----|------------------------------|
| 3D | 3-Dimensional |
| CFD | Computational Fluid Dynamics |
| DEM | Discrete Element Method |
| DOE | Design of Experiment |
| DPM | Discrete Phase Model |
| LBM | Lattice Boltzmann Method |
| MRF | Multiple Reference Frame |
| LES | Large Eddy Simulation |
| RPM | Round Per Minute |
| SD | Standard Deviation |
| SM | Sliding Mesh |

highly turbulent flow to lift them up and suspend them in the liquid phase [3]. Moreover, contra-rotating impellers also provide high static pressure, produce high pumping rates, and enhance performance in solid–liquid mixing. This type of mixing reactor has been invented to improve mixing proficiency in food processing, agriculture, and pharmaceutical industries [2,3]. In contra-rotating impellers, the rotation of impellers in opposite directions consists of two impellers arranged one above the other on nested, contra-rotating axes. The two axes are connected to a differential gearbox, which transfers power from the motor. In our previous publication [3], the contra-rotating impeller with different flow configurations (i.e., inward, outward, both up, and both down) were compared the mixing efficiency (how uniformly distributed the solid particles are) with a co-rotating impeller, both with and without baffles. The results show that the contra-rotating, baffle free impeller with inward opposing flow which gave optimal mixing performance at the lowest required torque. The computational fluid dynamics (CFD) model was used to predict the solid–liquid mixing in the mixing tank with different impeller types and flow patterns, as mentioned previously. All model configurations have been validated and show good agreement with the experimental data. In this study, the same type of mixing tank is employed to study the design parameters and to optimize

mixing and design guidelines for pitched-blade contra-rotating impellers with an inward flow configuration.

Several researchers have studied the effect of changing the design parameters in order to understand the variation of mixing time, uniformity, torque, and flow pattern in multiple impeller, single shaft (non-contra-rotating), baffled mixers [4–11]. These included the study of the rotation speed, impeller diameter, tank geometry, impeller clearance from the bottom, and the distance between the two impellers. The results of these studies revealed that the rotation speed and impeller diameter have the most impact on mixing uniformity (i.e., mixing efficiency in this work). The optimization of contra-rotating impeller, with feature inward flow pattern, is made here for the first time. The mixing efficiency, defined as how uniformly distributed the solid particles are within the tank, is used with the torque requirement to find the optimal design for this impeller.

Mechanisms of solid particle mixing and the mixing reactor design are complicated due to the influence of many variables such as relative density differences, particle size, rotation speed, impeller geometry, and tank geometry. These must be optimized. The Design of Experiments (DOE) is an approach used in engineering parametric studies to develop the expected product and engineering processes faster. A DOE can reduce

production costs and development time, while improving quality and reliability [12–15]. One of the common methods for DOE in engineering is the Taguchi method [16,17]. Several researchers [18–20] have applied the Taguchi method for reactor design optimization. However, no study to date has used it to optimize the design of an impeller type mixer. In this work, the Taguchi method was employed for the DOE. The goal of this study is to optimize a baffle-free, low torque mixer/reactor with contra-rotating impellers in an inward opposing flow configuration.

CFD is a numerical simulation/analysis technique that is used to analyze and solve engineering problems that involve fluid flows [21–23]. There were several studies on mixing reactor design using CFD with Lattice Boltzmann Method (LBM) [3,24,25], which can simulate mixing in liquid–liquid, solid–liquid, and gas–liquid systems. These include the study of solid particle or bubble flow dynamics in mixing tanks. Some researchers have used CFD with Discrete Element Method (DEM) and flow visualization techniques (electrical resistance tomography, ERT) to explore solid–liquid mixing operations [26,27], which can quantify the influence of each interaction force (i.e. lift forces, pressure gradient, and virtual mass) on simulation results. However, the relative impact of the control factors and control levels that affect mixing efficiency and torque is unknown. The present DOE study of parameters with CFD simulations and confirmatory experiments are able to explain the relationship between design parameters and control levels that affect the mixing efficiency and torque. With this study we present for the first time the optimized configuration of the pitched-blade contra inward-rotating impellers and have provided the design guidelines for their implementation in mixing devices.

In this work, the outcomes of DOE technique following CFD-LBM simulation is used to perform the design optimization of contra-rotating impeller with the inward flow pattern. The using of design of experiments can reduce the number of running full factorial analysis from 2,187 to 27 runs. The twenty-seven CFD simulation cases with different design parameters that studied are from the L_{27} orthogonal array. The three-dimensional (3D) CFD-LBM is used to predict the solid particles motion in the liquid phase by using the Discrete Phase Model (DPM). The tank image is used to calculate the mixing efficiency, where the image is analyzed to confirm the uniformity of the particle distribution. The analysis method is developed from the intensity of segregation method and coefficient of variation (CoV). The statistical approach, signal to noise (S/N) ratio, which indicates the robustness of design parameters is used with torque data for making a design optimization. The DOE allowed for the reduction of experimental and simulation runs and lead to the optimized configuration.

2. Taguchi design of experiment

The Design of Experiments (DOE) is a methodology for the design of any task to describe the relationship between input design variables or factors (i.e., rotation speed and tank geometry) affecting a process and the output variables (i.e., mixing efficiency and torque). DOE is proposed to find the possible schemes with the number of design variables and different variable levels for reducing the number of CFD simulations or experiments.

2.1. Taguchi robust design for mixing optimization

The Taguchi design was developed by Genichi Taguchi [16,17].

This method is used in optimizing the process of experimentation and reduces the number of experimental runs by using orthogonal arrays. An orthogonal array consists of a set of fractional factorial designs based on a design matrix, which means that the experiment design parameters or control factors are balanced so that factor levels are weighted equally [16,17,28]. Taguchi schemes are classified as a function of the number of experimental runs (La), the number of levels of each control factor (b), and the number of variables or control factor (c), resulting in the orthogonal arrays notation $La(b^c)$. Taguchi array or orthogonal array, for each level of the parameter, all levels (b) of each of the other parameters ($c-1$) are tested at least once.

For the mixing system, the key process related to high mixing efficiency and low torque is the appropriate design parameters. The dimensions of the mixer and impellers in this study are shown in Fig. 1a and b. The design parameters of tank and impeller geometry are the control factors those affect mixing efficiency and torque the most. The particular design parameters are: (1) Impeller rotation speed, RPM, (2) Impeller diameter, D , (3) Impeller-impeller clearance, S , (4) Impeller-bottom clearance, C , (5) Tank diameter, T , (6) Liquid height, H , and (7) Number of blades, N_B . These design parameters are chosen as the controlled inputs for the DOE in order to investigate their influence on mixing efficiency and torque [3,29–36]. Note that the liquid height (H) is considered as a controllable design parameter, representing the full capacity of the tank; that is, the effect of liquid level on the mixing efficiency and torque of the system is being investigated.

In general, of the Taguchi DOE, the full factorial analysis is used to manipulate the design of the experiment with a small number of control factors and control levels. For the present study, seven control factors ($c = 7$) were used. For seven control factors, the appropriate number of control levels are two and three [16]. So, three levels of each control ($b = 3$) were used to increase the accuracy of design of experiments. The design parameters and control level of each factor are shown in Table 1. The extrema were based on the operating limits of the pilot-scale mixer. The design of experiments using the Taguchi orthogonal array is more efficient compared to many other statistical designs. The minimum number of experiments that are required to conduct the DOE can be calculated based on the degrees of freedom by the following equation:

$$N_{Taguchi} = 1 + \sum_{i=1}^c b_i - 1 \quad (1)$$

where $N_{Taguchi}$ is the minimum number of experiments. In this study, for seven control factors with three control levels, the minimum number of experiments required, based on Eq. (1), is 15. Hence, the number of experiments for this study should be greater than 18 or $L_{18}(3^7)$. In this work, an $L_{27}(3^7)$ orthogonal array was used to perform the DOE. The full factorial analysis in this study is (3^7) 2,187 runs, and after applying the orthogonal array, the number of the runs is reduced to 27. The $L_{27}(3^7)$ orthogonal array with control factors and control levels is shown in Table 2.

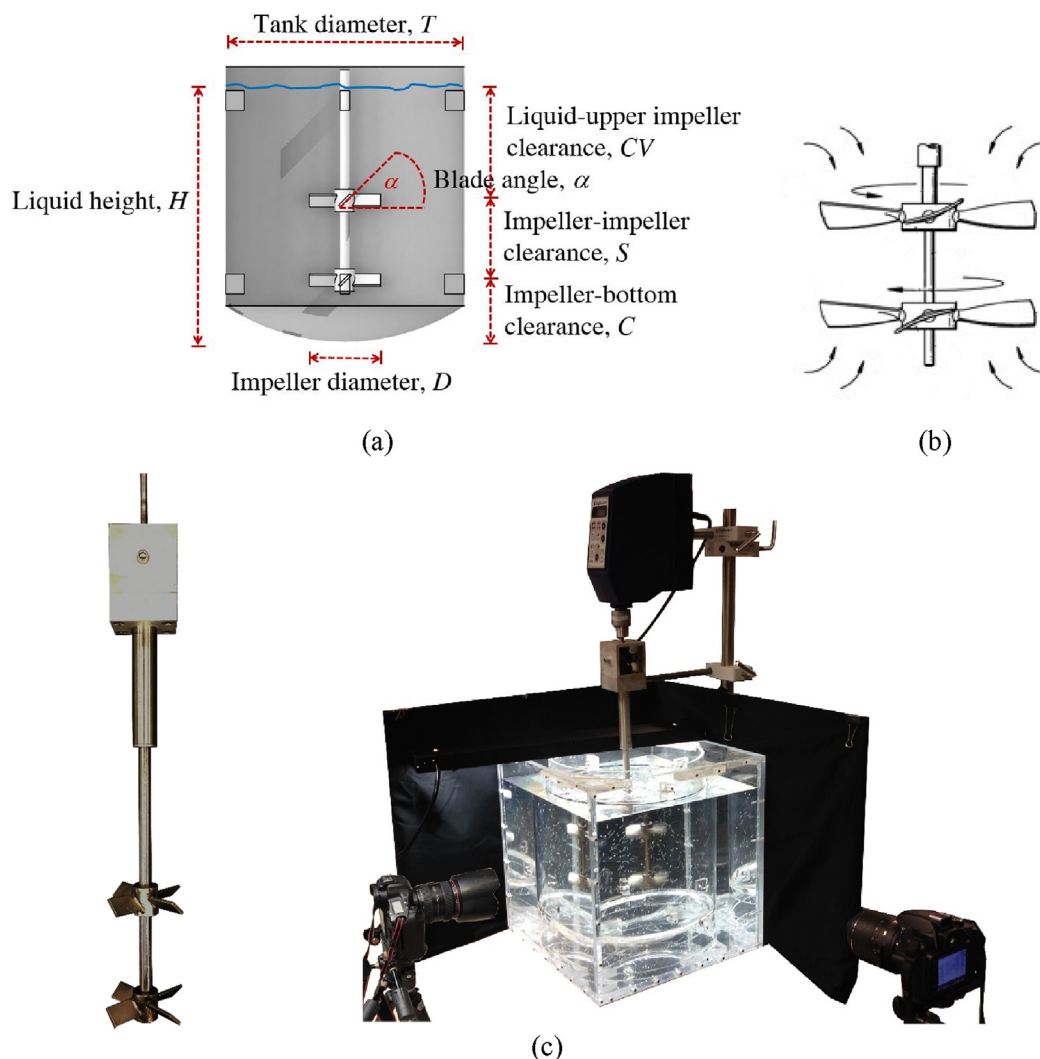


Fig. 1 (a) Dimensions of mixer and impellers in this study, (b) The flow configurations used in this study, and (c) Experimental apparatus used to evaluate torque and capture experimental data for optimization case (Case L4).

Table 1 Seven control parameters and three study levels.

| Control Factors | Level 1 | Level 2 | Level 3 |
|----------------------------------|---------|---------|---------|
| Rotation Speed (RPM) | 100 | 200 | 300 |
| Impeller diameter (mm) | 90 | 150 | 200 |
| Impeller-impeller clearance (mm) | 100 | 125 | 150 |
| Impeller-bottom clearance (mm) | 100 | 125 | 150 |
| Tank diameter (mm) | 300 | 350 | 400 |
| Liquid height (mm) | 300 | 350 | 400 |
| Number of blade (n) | 4 | 6 | 8 |

2.2. Experimental setup and procedure for model confirmation of the design optimization

The experimental setup for model validation is shown in Fig. 1c. This experiment will be only used to confirm the design optimization derived by the DOE in this work. It was

constructed from two tanks, a cylindrical tank with a round bottom and an outer rectangular tank to eliminate distortion, similar to the previous publication [3]. The cylindrical tank is 0.30 m in diameter and 0.35 m in height. The rectangular tank is 0.40 m in diameter and 0.40 m in height. Both tanks were filled with water to the same height to eliminate the image distortion. Two of 45° pitched-blade turbine impellers were installed in the center of the tank on the different shaft (i.e., two rotating axles) with the adjustable dimension. Both impellers are arranged one above the other on nested, contra-rotating axles. These two axles are connected to a differential gearbox [2], which transfers power from the motor. The impeller was stirred by a Caframo BDC 3030 rotator motor with speed controls and a torque sensor. The residual torque or the background torque was measured without water in the vessel. This setup had a residual torque of 0.0058 N.m, which can be considered as negligible.

Particles of higher and lower density than water were used; the higher specific gravity was 1.050 and had a diameter of 2.05 mm and the lower specific gravity particle of 0.866 had a diameter of 2.45 mm. A total of 500 particles were used

Table 2 L27 orthogonal array with control factors and control levels for this study.

| Trial number | Rotation speed (RPM) | Impeller diameter (mm) | Impellers clearance (mm) | Impeller-bottom clearance (mm) | Tank diameter (mm) | Liquid height (mm) | Blade Number (n) |
|--------------|----------------------|------------------------|--------------------------|--------------------------------|--------------------|--------------------|------------------|
| L1 | 100 | 90 | 100 | 100 | 300 | 300 | 4 |
| L2 | 100 | 90 | 100 | 100 | 350 | 350 | 6 |
| L3 | 100 | 90 | 100 | 100 | 400 | 400 | 8 |
| L4 | 100 | 150 | 125 | 125 | 300 | 300 | 4 |
| L5 | 100 | 150 | 125 | 125 | 350 | 350 | 6 |
| L6 | 100 | 150 | 125 | 125 | 400 | 400 | 8 |
| L7 | 100 | 200 | 150 | 150 | 300 | 300 | 4 |
| L8 | 100 | 200 | 150 | 150 | 350 | 350 | 6 |
| L9 | 100 | 200 | 150 | 150 | 400 | 400 | 8 |
| L10 | 200 | 90 | 125 | 150 | 300 | 350 | 8 |
| L11 | 200 | 90 | 125 | 150 | 350 | 400 | 4 |
| L12 | 200 | 90 | 125 | 150 | 400 | 300 | 6 |
| L13 | 200 | 150 | 150 | 100 | 300 | 350 | 8 |
| L14 | 200 | 150 | 150 | 100 | 350 | 400 | 4 |
| L15 | 200 | 150 | 150 | 100 | 400 | 300 | 6 |
| L16 | 200 | 200 | 100 | 125 | 300 | 350 | 8 |
| L17 | 200 | 200 | 100 | 125 | 350 | 400 | 4 |
| L18 | 200 | 200 | 100 | 125 | 400 | 300 | 6 |
| L19 | 300 | 90 | 150 | 125 | 300 | 400 | 6 |
| L20 | 300 | 90 | 150 | 125 | 350 | 300 | 8 |
| L21 | 300 | 90 | 150 | 125 | 400 | 350 | 4 |
| L22 | 300 | 150 | 100 | 150 | 300 | 400 | 6 |
| L23 | 300 | 150 | 100 | 150 | 350 | 300 | 8 |
| L24 | 300 | 150 | 100 | 150 | 400 | 350 | 4 |
| L25 | 300 | 200 | 125 | 100 | 300 | 400 | 6 |
| L26 | 300 | 200 | 125 | 100 | 350 | 300 | 8 |
| L27 | 300 | 200 | 125 | 100 | 400 | 350 | 4 |

for each experiment and simulation. This is the suitable number of particles to prevent particle obstruction and reduce the error from the image analysis [3]. The particle's movement in the tank was captured by two Nikon D3200 cameras to obtain two side-plane images every 0.50 s from 0 to 60 s. Upon completion of the experiment, the captured photographs of the tank were analyzed to obtain the mixing efficiency.

3. Numerical method

3.1. Lattice Boltzmann method (LBM)

The Lattice Boltzmann Method (LBM) is a numerical simulation technique capable of solving complex fluid flow problems including multiphase flow and free surface models with complex geometries and moving parts, such as occur over an impeller. LBM has many advantages over conventional CFD (i.e. Navier-Stokes equation) for modeling moving geometries such as rotating impeller. This method uses a lattice element instead of the traditional meshing process, which does not require the use of computational approaches such as Multiple Reference Frame (MRF) or Sliding Mesh (SM) to model moving parts in the mixing system. The LBM simulation relies on a generated lattice element, which is organized in an Octree structure, and uses a Large Eddy Simulation (LES) turbulence model, which can reduce meshing operation and computational times. The particle-based approach can easily handle

fluid domain meshing of a moving surface boundary. This method uses the concept of streaming and colliding particles, which incorporates the physics of microscopic and mesoscopic processes such that the macroscopic, averaged properties obey the applicable macroscopic equations [37–42]. The transport equation of this method is shown below.

$$f_j(\vec{x} + \vec{e}_j \Delta t, t + \Delta t) - f_j(\vec{x}, t) = \Omega_j(f_1(\vec{x}, t), \dots, f_m(\vec{x}, t)), \quad j = 1, \dots, m \quad (2)$$

where f_j is the particle distribution function in direction j , \vec{x} is the lattice node, \vec{e}_j is the particle discrete set of velocities, t is the discrete times, Δt is the constant time step, Ω_j is the collision operator, and m is the probability distribution function of the particle distribution function. The Boltzmann transport equation describes the statistical distribution of particles in the space, time, and velocity in the form of a particle distribution function. The LBM makes use of the statistical distribution function with real variables, conserving mass, momentum, and energy [39]. So, the continuum Boltzmann transport equation, macroscopic variables, such as velocity \vec{u} , and density ρ can be determined as the moments of the lattice particle distribution function, as shown in below:

$$\rho = \sum_{i=1}^b f_i \quad (3)$$

$$\rho \bar{u} = \sum_{i=1}^b f_i \bar{e}_i \quad (4)$$

The macroscopic fluid pressure (P), that represents the equation of state, can be calculated from the following equation:

$$P = \rho c_s^2 \quad (5)$$

The Taylor series with the multiscale Chapman-Enskog expansion provides the relation between the macroscopic kinematic viscosity and the relaxation parameter:

$$n = c_s^2 \left(\tau - \frac{1}{2} \right) \quad (6)$$

where n is the macroscopic kinematic viscosity, c_s is the speed of sound, τ is the relaxation parameter, and $\tau > \frac{\Delta t}{2}$ is a required stability condition. Note that the recommend relaxation parameter should stay within the range of 0.5 to 1.5 ($\tau = 0.5$ in this study). There are two different collision operators for LBM, single and multiple relaxation time (SRT and MRT). In this model, the MRT is used as a collision operator and can be approximated by the following:

$$\Omega_i^{MRT} = M_{ij}^{-1} \hat{S}_{ij} (\mu_i^{eq} - \mu_i) \quad (7)$$

where the collision matrix (\hat{S}_{ij}) is a diagonal relaxation matrix, μ_i^{eq} is the equilibrium value of the moment μ_i , and M_{ij} is a matrix that transforms the particle distribution function to the macroscopic moment. More details concerning the LBM and transport equation for this method were discussed in [Supplemental material](#) and previous publications [3,24,43].

In order to simulate the particle movement through the tank, LBM can be coupled with the Discrete Element Method (DEM) or Discrete Phase Model (DPM). This work used the DPM because this method is appropriate for hard-sphere collisions (i.e. solid–solid particles collisions) with no particle overlap [44]. The DPM is advantageous because it requires less computation time and data storage space than the DEM [41]. The DPM method solves the transport equation for the continuous phase and calculates the transport of a discrete phase consisting of spherical particles (i.e., droplets, dust, bubbles, etc.) dispersed in the continuous phase. The following is the equation of motion:

$$\frac{d\bar{u}_p}{dt} = \bar{a}_{D(f-p)} + \bar{a}_{Extf,p} + \bar{a}_{Ext,p} \quad (8)$$

where \bar{u}_p is the particle velocity, $\bar{a}_{D(f-p)}$ is the acceleration of the particle due to the drag force exerted by the fluid phase (f) on the particle disperse phase (p), $\bar{a}_{Extf,p}$ is the external acceleration affecting both phase (f, p), (e.g. gravity), and $\bar{a}_{Ext,p}$ is the external acceleration affecting only disperse phase (p).

3.2. Computational model

Three-dimensional, time-dependent simulations of mixing and agitation system with a free surface model were run for 27 cases with different designs, as shown in [Table 2](#). The mixer geometry involves a tank and a contra-rotating impeller. The mixing models were distinguished by rotation speeds of 100, 200, and 300 RPM. The mixing tank has a round bottom with

a cylindrical shape with different sizes depending on the arrangement of the orthogonal array. Two impellers have four, six, and eight pitched-blades turbine (PBT) at 45 degrees (4, 6, and 8 PBTs) with different diameters and mounting on the same shaft. The contra-rotating systems have two impellers rotating in opposite directions. The Euler angle with the moving wall bounce-back boundary condition was used on the impeller part. It allows the impellers rotate around its own axis and each direction. The moving wall assumption is used to apply the bounce-back rule for the non-equilibrium part of the particle distribution function normal (f_j) to the boundary. A no-slip condition was defined at all surfaces of the tank, and the free-surface boundary was imposed in the function of liquid height. The rotation speed (n) is related to the Reynolds number (Re) and the Euler angle. A rotation system Reynolds number [45] can be defined as follow:

$$Re = \frac{\rho n D^2}{\mu} \quad (9)$$

where Re_S is the Reynolds number for rotation system, D is the impeller diameter, n_r is the rotation speeds (RPS), and μ is the molecular viscosity of the fluid. The Reynolds number employed in this study is in the range of 100,000 to 200,000, which is in the turbulent region. The dimensionless power number (N_p) relating the resistance force to the inertial force is one of the most widely used design specifications in mixing operation. The power number for a stirred tank is defined as:

$$N_p = \frac{P}{\rho n^3 D^5} \quad (10)$$

where P is the power required by the impeller, which is calculated from measurements of the torque and impeller speed:

$$P = 2\pi n T_r \quad (11)$$

where T_r is the torque (N.m). The torque is defined as the measure of force required to produce rotational motion. In general, torque is calculated by multiplying the force by the distance from the pivot point to the point where the force is applied. In this numerical simulation, the torque calculation is based on an angular momentum balance on the control volume surrounding the impeller [46,47]. This method uses the velocity profiles around the impeller to calculate the force, which is used to calculate torque, as shown in the following equation:

$$T_r = \int_{Control\ surface} \rho (\vec{V} \cdot \vec{n}) (\vec{r} \times \vec{V}) dA \quad (12)$$

where \vec{V} is the fluid velocity (m/s), \vec{n} is the unit normal vector at the control volume surface, and \vec{r} is the radius vector of propeller (m). The blade tips speed of impeller is calculated from the following equation:

$$T_{ps} = \pi D n \quad (13)$$

where T_{ps} is the Blade Speed (tip speed), measures how far a point on the outer most edge of the disperser blade travels at a given amount of time.

For the 3D model used in this work, a commercial LBM solver, XFlow 2019x (Build 106.00) [48], was chosen to perform the calculation. This solver uses 3 spatial dimensions and 27 discrete velocities (i.e. D3Q27). The grid independent

study of CFD simulation was tested for sensitivity [3]. Lattice sizes of 0.5, 1, 2, and 3 mm were chosen to perform the grid independence study. The mixing efficiency, average liquid velocity, liquid–liquid concentration profiles, and torque are used to perform the grid independence study. The results show that the study variables have an error of about $\pm 3\%$ that are in an acceptable range. Therefore, in this study, the lattice element size was set at 2 mm, giving a total number of about 2 to 8 million elements, depending on the size and resolution of the computed geometry. The time step was calculated considering the initial maximum velocity (i.e., 1 m/s) and pressure gradient in the domain. So, the time step was set at 0.00012 s with a 60-second analysis time. The data frequency was set at 50 Hz for taking a simulation results every 0.02 s.

As mention previous, DPM was used to simulate the particles dispersion through the fluid in the tank. In this study, the solid particles of lower and higher density than water were used. The solid particles have the following properties: spherical shape, specific gravity of 0.866 or 1.050 $\text{g}\cdot\text{cm}^{-3}$, particle diameter of 2.45 mm or 2.05 mm, respectively, and total number of 500. The feeding point is located on the bottom of the tank for high specific gravity particles and on the top of the liquid surface for low specific gravity particles. The system starts feeding the particles when the simulation starts.

3.3. Model validation and grid independent study

The model validation of this CFD simulation has been conducted with the experimental data, which is already published as shown in Ref. [3]. In the previous work, the prediction of velocity distribution, power input of agitators (stirring torque), and mixing efficiency have been validated with the experimental data. There were twenty-four cases of comparison between computational model and experiment. The solid particle properties were also the same as in this work. From the overall validation, the simulation results showed good agreement with the experimental data. In this work, the model validation was conducted for Cases L1 and L4 to confirm the accuracy of simulation. The grid or lattice voxel independence study was also performed. This method was used to confirm that the solution is independent of the mesh resolution [49–51]. The lattice size of 0.5, 1.0, 2.0, 3.0, and 4.0 mm were compared to ensure that the lattice voxel size did not affect the model predictions including mixing efficiency and torque. These CFD simulations were calculated in Case L4 with the rotational speed of 100 rpm and analyzed at the same time step. The result of grid independent study is reported in Table 3. The predictions show that there is slight change in the mixing

efficiency, average blade tips velocity, velocity profiles, pressure drop across the tank, power number, and stirred torque present inside each simulation, especially at the lattice size < 2.00 mm. So, a lattice size of 2.0 mm was determined to be acceptable and used in this work.

4. Image analysis

A transparent mixing tank with low volume fraction has the advantage of being able to track individual particles subject to the complexities of buoyancy. The image analysis method employed was developed from a statistical technique with the degree of deviation and is discussed in Supplemental material and a previous publication [3]. This method is an extension of the image analysis method developed from the coefficient of variation (CoV) and scale of segregation method [1,26,27]. Validation of this method has been completed by comparing to data from CFD simulation results and experimental data. The standard deviation (SD) between the experimentally measured data and CFD simulation data is in the range between 0.026 and 0.090. The mixing efficiency (eff) presented in this work is an indicator that justify the uniformity of particles dispersion in the mixing tank, which is calculated based on the dispersed area of particles. The deviation from ideal mixing (s_k) is calculated individually for each horizontal (h) and vertical (v) region as the square root of the sum of square differences between the ideal particle fraction (f_{ideal}) and actual particle fraction (f_{act}) as shown below:

$$s_k = \sqrt{\sum (f_{ideal} - f_{act})^2}, k = h, v \quad (14)$$

This calculated actual particle fraction from those images accounts for the area of solid particles per the area of fluid. The worst case (s_k^*) is taken when all of the particles are in the smallest region, thus maximizing the deviation from ideal. The degree of deviation (δ_k) is calculated as one minus half the ratio of s_k and s_k^* shown in the below equation:

$$\delta_k = 1 - 0.5 \left(\frac{s_k}{s_k^*} \right)^2, k = h, v \quad (15)$$

The range of Eq. (15) will be between 0.5 (poor mixing) and 1 (near-perfect mixing). The flow and particles movement inside the reactor of both specific gravities reaches steady state after 30 s. Therefore, the steady state mixing efficiency was calculated using the average data of the mixing efficiency after 30 s. The mixing efficiency is defined in Eq. (16) as the fraction of particles visible and the average product of the degree of

Table 3 Grid independence study information.

| Lattice size (mm) | Average tips velocity (m/s) | Torque (N.m) | Power number | Pressure drop (Pa) | Mixing efficiency (%) |
|-------------------|-----------------------------|--------------|--------------|--------------------|-----------------------|
| 4.00 | 0.93 | 0.028 | 0.83 | 4,381 | 80 |
| 3.00 | 0.81 | 0.025 | 0.74 | 3,592 | 81 |
| 2.00 | 0.62 | 0.023 | 0.69 | 2,878 | 85 |
| 1.00 | 0.59 | 0.022 | 0.68 | 2,735 | 83 |
| 0.50 | 0.61 | 0.022 | 0.68 | 2,936 | 85 |

deviation in the horizontal plane (δ_h) and vertical plane (δ_v) direction over the two planes. A quadratic function was chosen to keep a low gradient for slight deviations, making the combined penalty non-linear.

$$eff = \frac{N_{vis}}{N_{ideal}} \cdot \delta_v \cdot \delta_h \quad (16)$$

where N_{vis} is the number of particles visibly drawn into the liquid, and N_{ideal} is the total number of particles were fed into the liquid. (Other variables such as torque, uniformity, shear stress, or velocity profiles can be investigated independently but are here subsumed in the mixing efficiency.) The maximum solid volume fraction in this work that can be detected by this image analysis is 0.115.

The advantage of using this method is that it can be performed for a number of planes, a variety of tank divisions that need not be uniform, and on experimental and computational systems alike. Limitations of this technique are when a large number of particles diminishes transparency of the system, or when a significant amount of gas bubbles visually imitates the particles.

5. Result and discussion

5.1. Torque and power number

Fig. 4a and b report CFD predictions of torque with mixing efficiency and power number for both types of particle for all 27 mixer configurations. The results show that the impeller diameter has a strong effect on the torque at the same rotation speed. Impellers with long blades would provide more thrust but require more torque to stir the system. The number of blades has a large impact on the torque at the largest impeller diameter but has little effect on the smaller impeller diameter. In the pilot scale, the impeller diameter shows the most impact on power number. There is slight change of torque in this work (i.e., range between 0.05 and 0.6 Nm). From Eq. (10), it shows that the impeller diameter has the most significant effect on power number. The small impeller diameter has a higher power number than that of the large impeller. Note that the power number was calculated at the fixed rotation speed for each case followed by the design from Table 2. The addition of the extra blades causes increased drag force, which requires more torque at the same rotation speed. Since lower rotation speed is better, the RPM drop and the fluid velocity will tend to drop with it. Therefore, when increasing from 4 to more blades, the impeller diameter should reduce an inch or more in order to maintain similarity of torque.

Higher torque occurs with vortex formation in the contra-rotating impeller, whereas in the co-rotating impeller without baffles tank [3], vortex formation decreases torque. This is because the vortex that occurs in the contra-rotating impellers represent extremely turbulent flow in the mixing tank. It is noted that the torque required for each system does not have a direct relation to mixing efficiency. The optimized design should have the highest mixing efficiency at the lowest torque and power number. Cases L4 and L5, and L9 have the mixing efficiency more than 80% for both types of particle and Case L4 gives the lowest torque and power number from those three cases. Therefore, L4 is deemed the optimal design and it was chosen to perform confirmatory experiments.

5.2. Confirmatory experiments

The confirmatory runs for LBM-CFD regarding the investigation of mixing with contra-rotating impeller were discussed in previous work [3]. In the present work, this method of exploratory will be used to confirm the results of the DOE optimization. Case L4 is selected for confirmation because it has a good mixing efficiency, low torque, uniform particle dispersion, and operates at low RPM that is experimentally easy to reproduce. Based on this configuration, the optimal mixer unit was experimented, and the mixing efficiency calculated. Case L4 represents the optimal mixing tank, which is operated at 100 RPM. This tank has a diameter of 300 mm with the liquid level of 300 mm. The impeller has a diameter of 150 mm with 4 blades and both impellers clearances (C , S) are 125 mm. Fig. 5 shows the transient simulation and experimental mixing efficiency of Case L4 for the two specific gravity particles. The experimental set up is the same as the CFD simulation of Case L4, as mentioned previously. The particle movement in the tank was captured by two cameras to obtain two side plane images; these images were processed to quantify the mixing efficiency for comparison to the CFD simulation results.

Fig. 5a presents the mixing efficiency comparisons at lower specific gravity (SG 0.866) of Case L4 from times of 1 to 40 s. The predicted mixing efficiency is somewhat higher than the experiment data. The experimental observation presents mixing efficiency of 70%. The CFD simulation shows solid particles dispersed over more than 80% of the liquid domain. It was seen that experimentally tweaking the rotation speed to 110 RPM, brings the CFD simulation and the experimental mixing efficiencies into virtual agreement. The comparison of simulated and experimental mixing efficiency is shown in Fig. 5b for the high specific gravity particles. Visual observation shows that the particles begin to move up from the bottom of the tank then scatter throughout. The results show that the mixing efficiency from experiment is higher than the prediction during an initial transient from 0 to 8 s. Thereafter the mixing efficiency of the CFD simulation is higher than the experimental data, from times of 10 to 30 s. After 30 s, mixing efficiency from both the simulation and experiment are similar, with an error of about 6%. With this configuration, there is no vortex observed on both CFD simulation and experimental data.

5.3. Flow characteristics in the mixing tank

Figs. 2 and 3 present the solid particle dispersion and mixing efficiencies in the different mixers tested for Cases L1 to L27. The 2D pictures were captured in the front of the stirred tank at 40 s with 500 particles of low and high specific gravity, respectively. Each stirred tank has a different design geometry, which depends on the parameters that are defined by the L27 orthogonal array shown in Table 2. There is an order of the importance of design parameters influencing the mixing efficiency; rotational velocity is the first [3,24], then impeller diameter (D), and then impeller-impeller clearance (S). Therefore, the cases studied are divided into three main groups according to the rotational speeds of 100, 200, and 300 RPM. The sub-groups are divided into impeller diameters of 90, 150, and 200 mm. The steady state mixing efficiency of each case was calculated from the average of mixing efficiency after 30 s. Mixing trends can be seen qualitatively by visual observation,

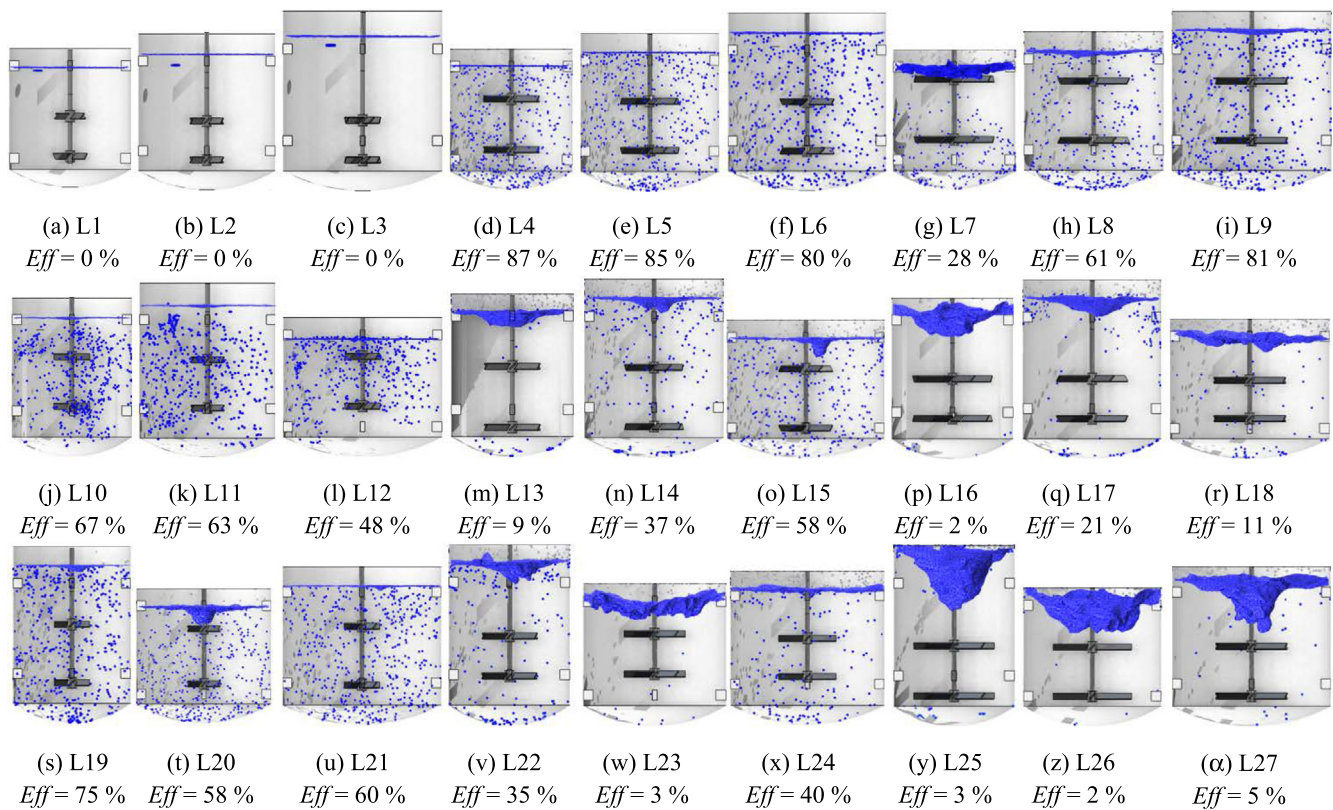


Fig. 2 CFD simulation of solid particles dispersions inside the stirred tank and mixing efficiencies compared in different mixer designs and operating conditions at 40 s at low specific gravities.

and these are confirmed by quantitative assessment of mixing efficiency which is the basis for design optimization.

5.3.1. Effect of mixer dimension at low rotation speed (Cases L1 to L9)

Figs. 6 and 7 present the transient CFD simulation mixing efficiencies of Cases L1 to L9 at lower and higher specific gravity, respectively. In these cases, the rotation speed was set at 100 rpm and the ratio of the liquid height to the tank diameter (H/T) is 1. Cases L1 to L3 have the same impeller diameter (D) of 90 mm with the same clearance of both impellers (S , C) of 100 mm. These cases have different blade numbers of 4, 6, and 8 with liquid height (H) the same as tank diameters (T) of 300, 350 and 400 mm, respectively, as shown in Figs. 2a-c and 3a-c. At a lower specific gravity, the CFD simulation shows that there is no mixing occurring in the reactor (Fig. 6a); all particles were floating at the liquid surface for these cases. To confirm these results, an experiment was performed with the same setup as Case 1. The experimental results agree with the CFD simulation data, where no particles migrated down from the top of liquid surface and there is no particle movement inside the tank as seen in the CFD results in Fig. 2a. A lack of flow in the top liquid region is caused by the low rotational speed and the low ratio of the impeller to the tank diameter ($D/T < 0.4$). Another reason for poor mixing in cases L2 and L3 is the impeller level or impeller-bottom clearance (C), which is installed too low. For a higher specific gravity, the results also show poor mixing efficiencies in these cases, as seen in Fig. 7a. To confirm these CFD simulation results, an experiment was

performed again with the same set up as Case L1 but at higher specific gravity. The experimental data showed no mixing occurred in Case 1. CFD simulations do show, however, that cases L2 and L3 have some particle dispersion in the lower region of the liquid domain with the mixing efficiencies of 2% and 34%, as seen in Fig. 3b and c. Case L3 has more mixing efficiency than Case L1 and L2. This is because the impeller 8 blades, which can generate more flow in this area even though it is installed too low.

Figs. 2d-f and 3d-f present solid particle movement and mixing efficiency for Cases L4 to L6. The mixing efficiency for both specific gravities of these cases are reported in Figs. 6b and 7b. These cases have an impeller diameter (D) larger than the previous cases, 150 vs. 90 mm. Tank diameters, liquid height, and blade numbers were the same order as previous cases. The clearance of impeller-bottom (C) and impeller-impeller (S) were increased for 25 mm. The results reveal that the mixing efficiency is significantly increased after enlarging the impellers size, which results in improved flow, more turbulence, and favorable mass transport inside the tank. Visual observation confirms no vortex formation in these cases. The particle distribution in the mixer reaches steady state and is uniform after 12 s for both specific gravities. The mixing efficiency profiles show a steady trend for all cases, which is a representation of uniform particle distribution inside the tank. The mixing efficiency of these cases at lower specific gravity are 81%, 85%, and 80%, respectively. At the higher specific gravity, the mixing efficiency of these cases are 87%, 87%, and 78%, respectively. According to these

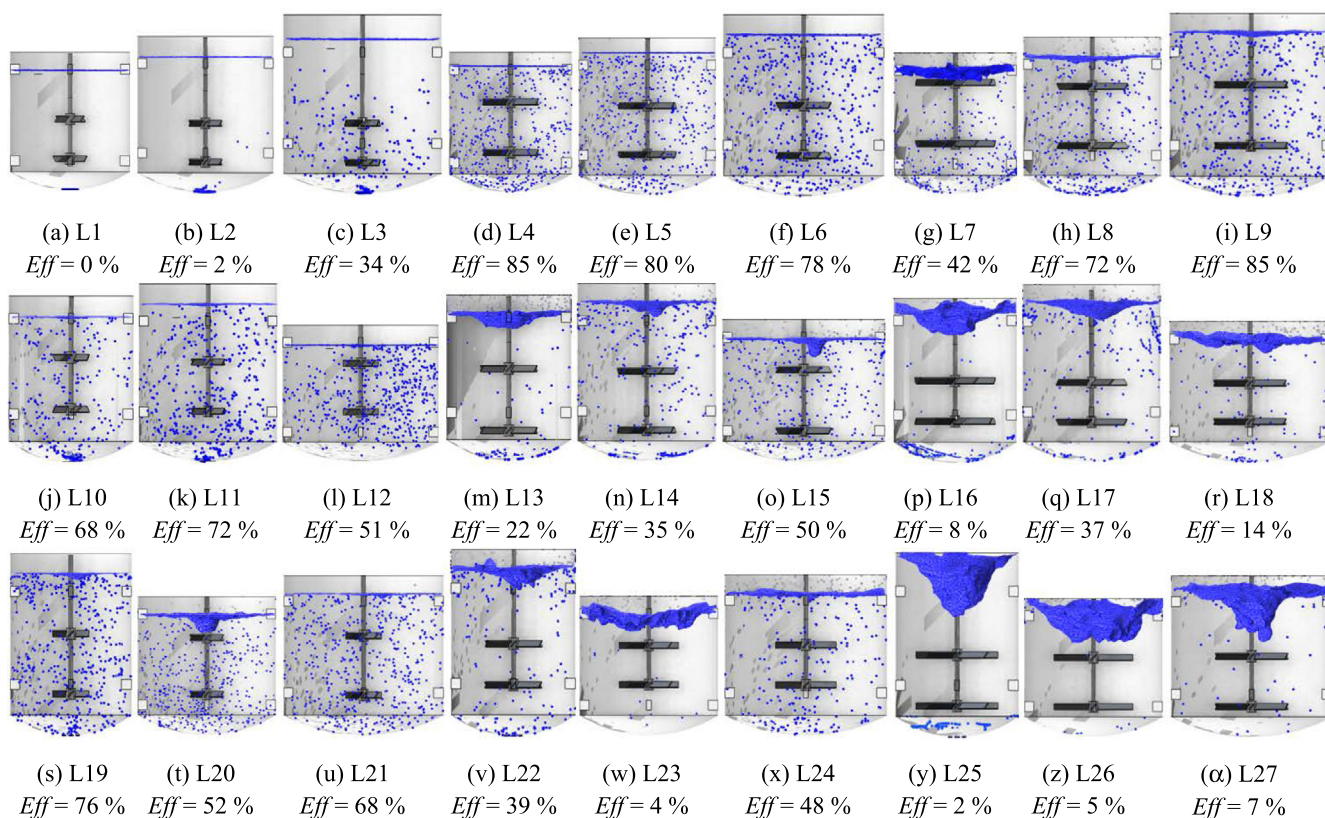


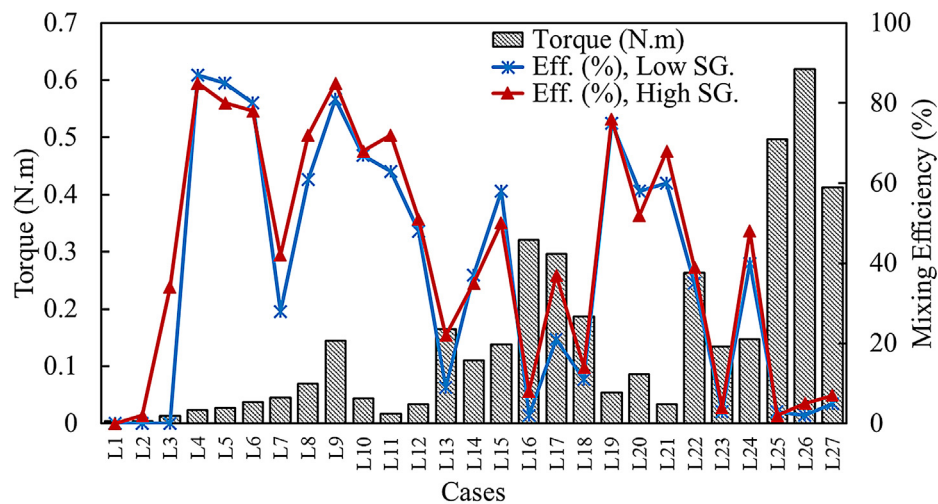
Fig. 3 CFD simulation of solid particles dispersions inside the stirred tank and mixing efficiencies compared in different mixer designs and operating conditions at 40 s at high specific gravities.

results, the suitable ratio between impeller to the tank diameter (D/T) should be in the range of 0.4–0.5 and the ratio of liquid height to the tank diameter (H/T) should be 1. What is interesting about Case L6 is it has a low D/T ratio of 0.38 in the largest tank (400 mm × 400 mm). Case L6 operates at 100 RPM with 8 blades. The result shows good mixing efficiency and uniform particles dispersion for both particle types in this study. This is because of more blades that can generate more axial flow and provide good mass transport, but this case needs more power to operate the system, as the torque increases in by 35%–50%. Thus, the optimal design for this group is Case 4, which has good mixing efficiency, operates at low RPM, and has lower torque.

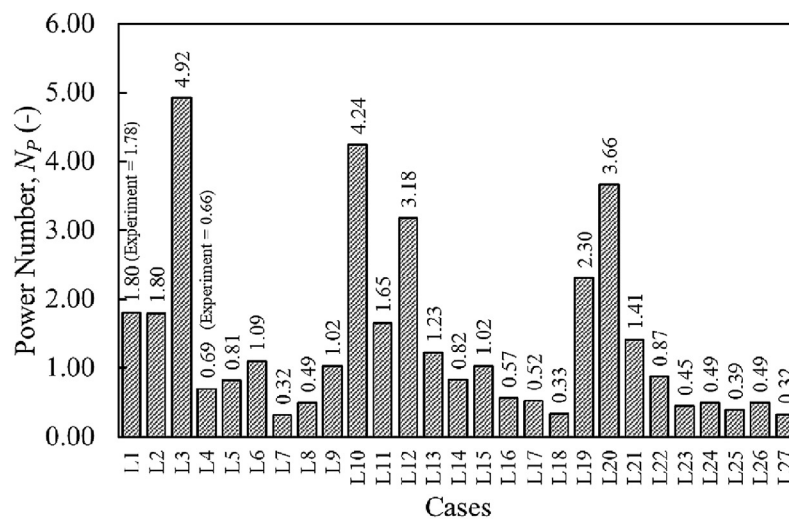
Cases L7 to L9 have increased impeller diameter (D) of 200 mm and increases of both clearances (S , C) to 150 mm, as shown in Figs. 2g-i and 3g-i. Tank diameter and blade numbers are in the same order with the previous cases. The mixing efficiency of light and heavy particle studies are presented in Figs. 6c and 7c. Visual observation of Case L7 shows that most of the water and some of the particles splashed out of the tank and mixing is poor for both particle types, 28% for lower specific gravity and 42% for higher specific gravity. This is because of too-large impeller diameter and too-high impeller installation in the small tank. Experiments were performed to confirm the CFD results and find the rotational speed limit (to prevent spillage) for the largest impeller. Water and particle spillage were observed at 100 rpm and became severe at 150 RPM.

Case L8 shows better mixing efficiency than Case L7 in the larger tank, which has a mixing efficiency of 60% for lower specific gravity and 72% for higher specific gravity. The results show acceptable particle dispersion without water spillage for both particle sizes. At lower specific gravity, the particles moved down from the top of liquid surface and then separate into two layers on the top and the bottom of the tank, as shown in Fig. 2h. This may be the large spacing between two impellers (S), which results in lack of flow around the middle area of the tank. However, the higher specific gravity case shows uniform particle dispersion, which is the effect of the gravity force affecting the particles. Case L9 is the largest volume and the highest liquid level in this study, as shown in Figs. 2i and 3i. CFD simulations present uniform particles dispersion and provide adequate mixing efficiency of 81% for lower specific gravity and 85% for higher specific gravity. The mixing becomes steady in 10 s, which is the fastest case of all, due to the high turbulent flow generated from 8 blades. However, the result shows that this case has the highest torque in this group (Cases L1 to L9), for operation at 100 RPM.

The summary of mixing efficiency of the 100 RPM runs is shown in Figs. 6d and 7d. Again, these tanks have a ratio of liquid height to the tank diameter (H/T) of 1. Cases L4, L5, and L9 illustrate uniform particle dispersion and provide mixing efficiencies greater than 80%. The rotational speed and the ratio of impeller diameter to the tank diameter (D/T) have the most influence on the mixing efficiency. The next important design parameter is the ratio of D/T . The recommend D/T of



(a)



(b)

Fig. 4 (a) CFD simulation of torque (N.m) with mixing efficiency (%) for twenty-seven reactor designs, and (b) CFD simulation of Power number for twenty-seven reactor designs.

these selected cases is about 0.45–0.50. If the mixer operates at higher rotational speed than 100 RPM, the ratio of D/T should be lower than 0.45. In these cases, low mixing efficiency occurs if the D/T ratio is lower than 0.40. The worst cases of this group are L1 to L3 which operate at low RPM and low ratio of D/T ($D/T < 0.30$), and gave virtually no particle dispersion or mixing.

5.3.2. Effect of mixer dimension at medium rotation speed (Cases L10 to L18)

The next cases, L10 to L18, investigated an increased rotating speed of 200 RPM. Figs. 2j-r and 3j-r present particle dispersion with the mixing efficiency of these cases. These mixers have a variety of geometries. The overall mixing efficiency with time is reported in Figs. 8 and 9. Figs. 2j-l and 3j-l present the mixing of Case L10 to L12 with mixing efficiency of 67%, 63%, and 48% for lower specific gravity, and 68%, 72%, and 51% for higher specific gravity. These cases have the

smallest impeller diameter with different numbers of blades 8, 4, and 6, respectively. These designs have impeller-impeller clearance (S) of 125 mm and the impeller-bottom clearance of 150 mm. The D/T ratio of these cases are 0.30, 0.26, and 0.23, respectively. In the previous cases L1 to L3 at 100 RPM there was no mixing. However, at a rotational speed of 200 RPM, mixing efficiency increases to more than 50%. This shows that the rotational speed plays a major role in the mixer design. Another reason for improving the mixing efficiency is more optimal clearances for the impellers (S , C). The appropriate installation level of both impellers should be in the middle of the liquid level. For example, cases L10 and L11 have both impellers installed around the middle of liquid level with the ratio of impeller bottom clearance to the liquid height (C/T) about 0.4. Both cases have a noticeably better mixing ratio than cases L12, which has the impeller level set to high. Although these cases have better mixing efficiencies, the overall mixing efficiency is still low. This is due to the low D/T ratio, which is lower than 0.40. The results also show

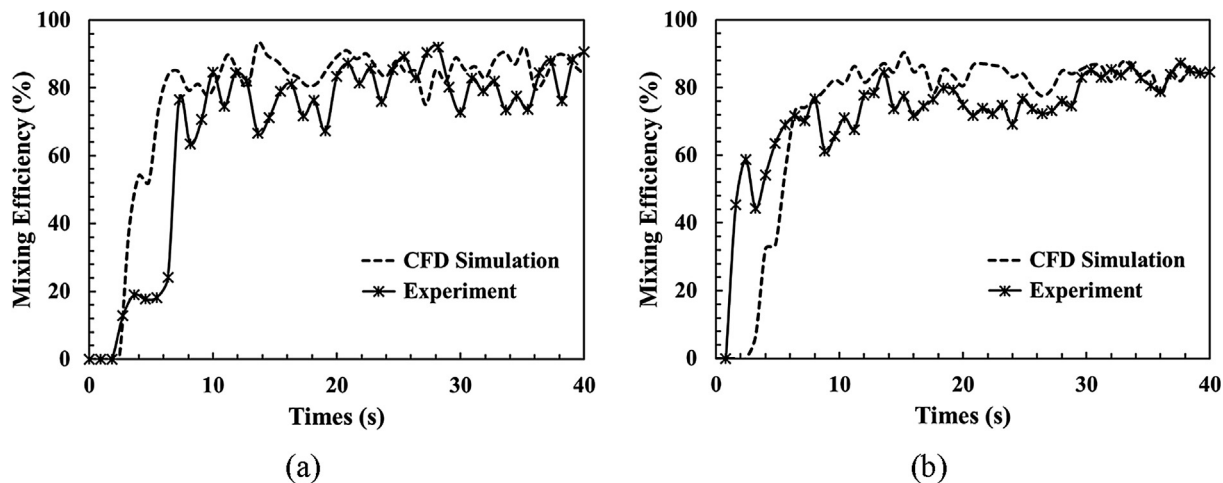


Fig. 5 CFD simulation and experimental of mixing efficiencies compared in Case L4 at (a) low, and (b) high specific gravities at a rotational speed of 100 RPM.

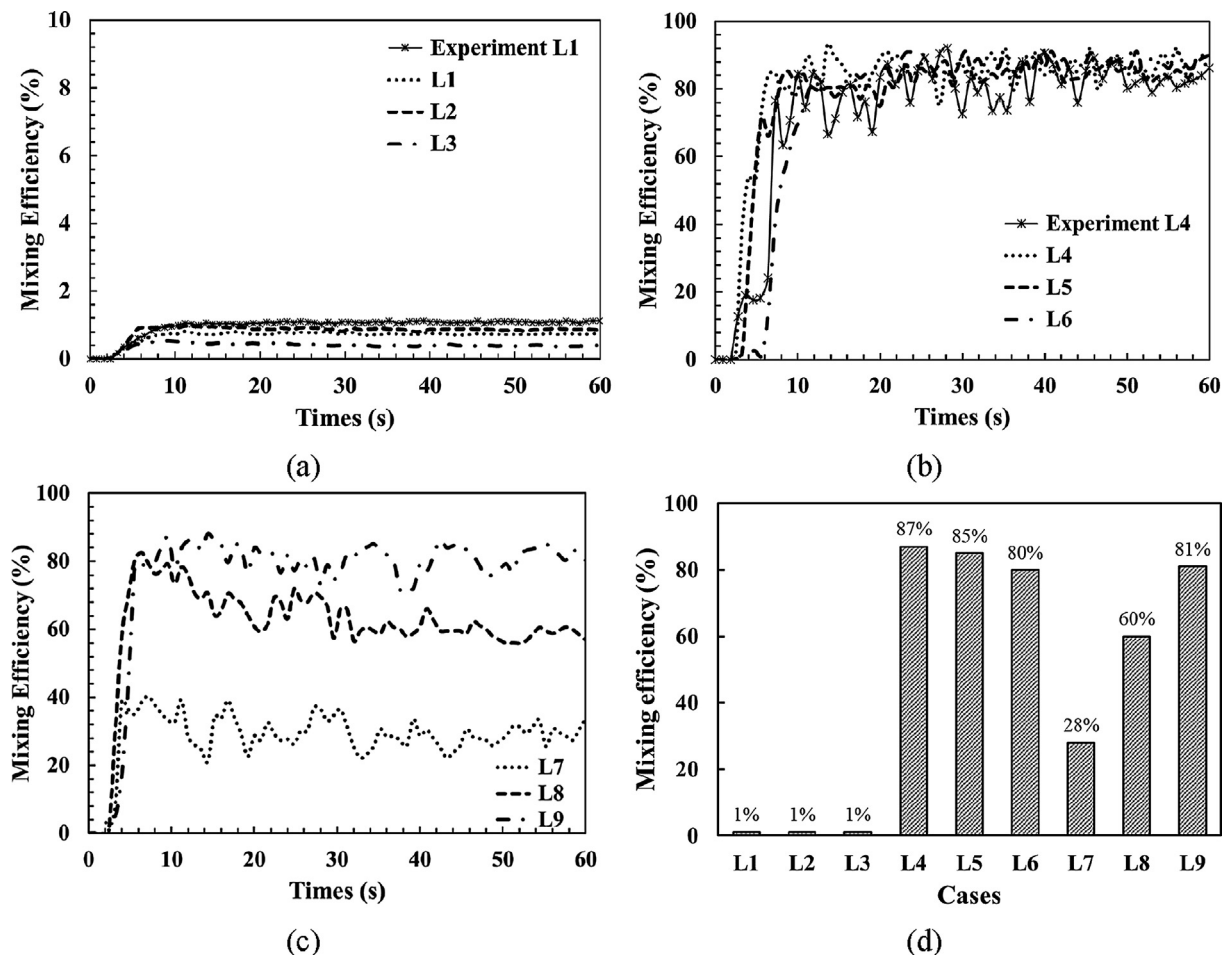


Fig. 6 CFD simulation of mixing efficiencies at lower specific gravity at rotation speeds of 100 rpm for the Cases L1 to L9, (a) Cases L1 to L3, (b) Cases L4 to L6, (c) Cases L7 to L9, and (d) Mixing efficiencies compared for the Cases L1 to L9.

that the mixing efficiency at the higher specific gravity slowly increases after 20 s, as shown in Fig. 9a. This is because the high impeller-bottom clearance (C) and high liquid level (H) effect the flow development around the bottom of the tank.

The mixing efficiency becomes steady after 30 s, which is representative of fully developed turbulence throughout the tank. Cases L13 to L15 have the same tank geometry as cases L10 to L12, as shown in Figs. 2m-o and 3m-o. These cases have the

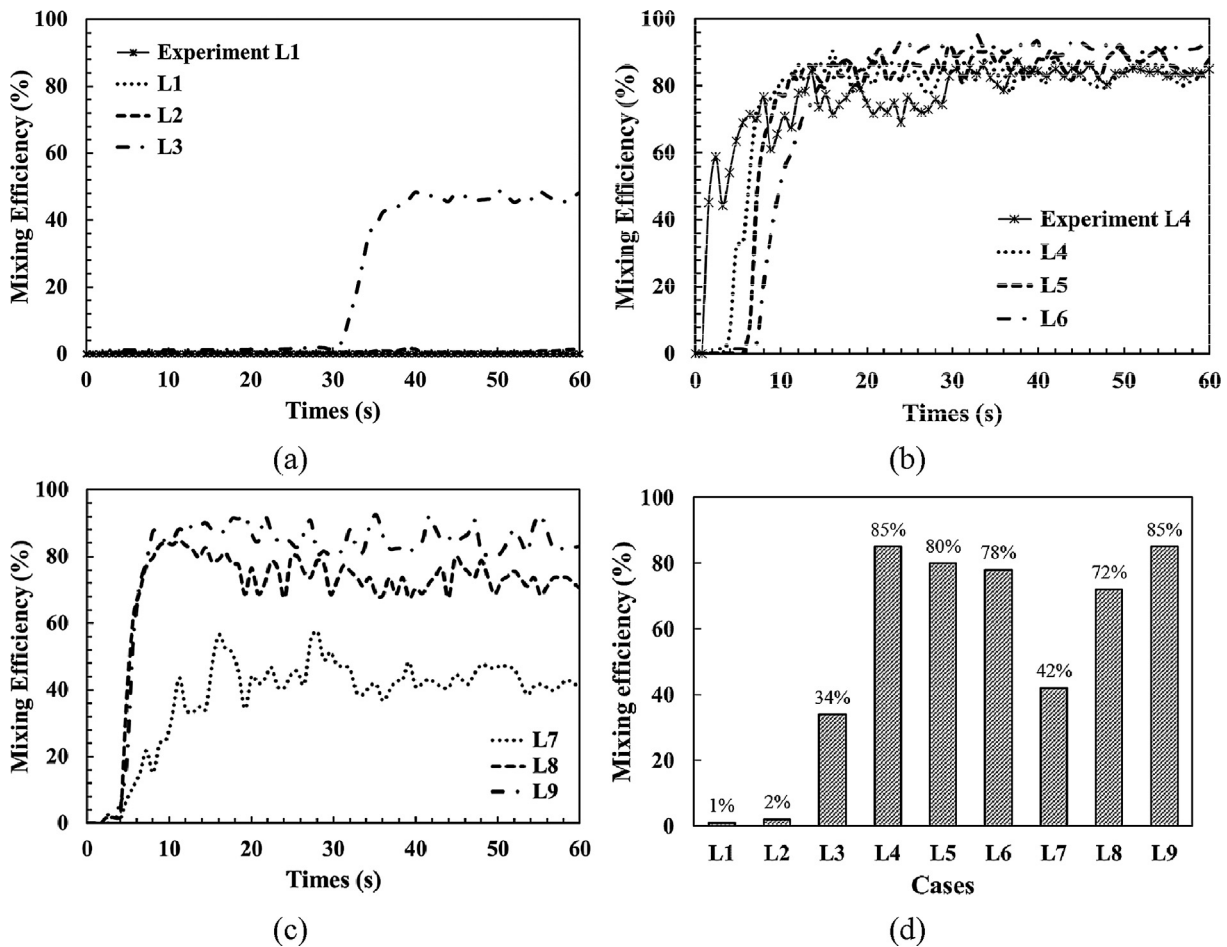


Fig. 7 CFD simulation of mixing efficiencies at higher specific gravity at rotation speeds of 100 rpm for the Cases L1 to L9, (a) Cases L1 to L3, (b) Cases L4 to L6, (c) Cases L7 to L9, and (d) Mixing efficiencies compared for the Cases L1 to L9.

same number of blades but a larger impeller diameter than previous cases. The impeller-bottom clearance (C) is 100 mm from the bottom of the tank, which is too low for cases L13 and L14 that have high liquid level. The clearance between two impellers of these cases are 150 mm. The mixing efficiency profiles of both specific gravities are shown in Figs. 8b and 9b. The mixing efficiency at lower specific gravity for these cases are 9%, 37%, and 58%, respectively. The mixing efficiency at higher specific gravity for these cases are 22%, 35%, and 50%, respectively. If the upper impellers are installed too low and high rotational speed is used, as seen in cases L13 and L14, a vortex forms at the liquid surface, and this creates bulk flow inside the tank. Since these cases have larger impellers, L13 and L14 provided lower mixing efficiency than cases L10 and L11 for both specific gravities. The vortex and bulk flow inside the tank cause efficiency to slightly decrease with time, as shown in Figs. 8b and 9b. This indicates that vortex formation is the main problem in the mixer designs. Case L15 shows mixing efficiency of more than 50% for both specific gravities in a short wide tank, but the relative mixing efficiency is not high. This case has high clearance between two impellers (S), which causes a lack of flow around the middle of the tank. The low ratio of D/T will lead to a lack of flow around the wall and cause a lower particles distribution on that area.

Figs. 2p-r and 3p-r present Cases L16 to L18. These have the largest impellers and the lowest impeller-impeller clearance (C) for this study. The tank geometry and number of blades are the same order as the previous cases. The mixing efficiency profiles at lower specific gravity of these cases are shown in Fig. 6c with a mixing efficiency of 2%, 21%, and 11%, respectively. The mixing efficiency profiles at higher specific gravity are reported in Fig. 9c with a mixing efficiency of 8%, 37%, and 14%, respectively. Case L16 shows low mixing efficiency for both specific gravities. The results from the experiment and CFD simulation show huge vortex formation and uncontrolled mixing inside the tank, as shown in Figs. 2p and 3p. According to the experiment, the rotating speed of this impeller size in the small tank has a limit of 125 RPM. This case has 8 blades and operates at 200 RPM, which is over the limit for the experiment. Visual observation shows that most of the particles and liquid water inside the mixer are spilled, which results in a low mixing efficiency. Case L17 is the medium tank diameter with the highest liquid level. The low installation level of the impeller can prevent water spillage, but it will lack the flow around the top of the tank area and cause vortex formation. This case shows smaller vortex size than Case L16 because it has fewer blades, which results in lower flow and velocity inside the tank. The result is that the particles are separated into two layers, located at the top and bottom of the

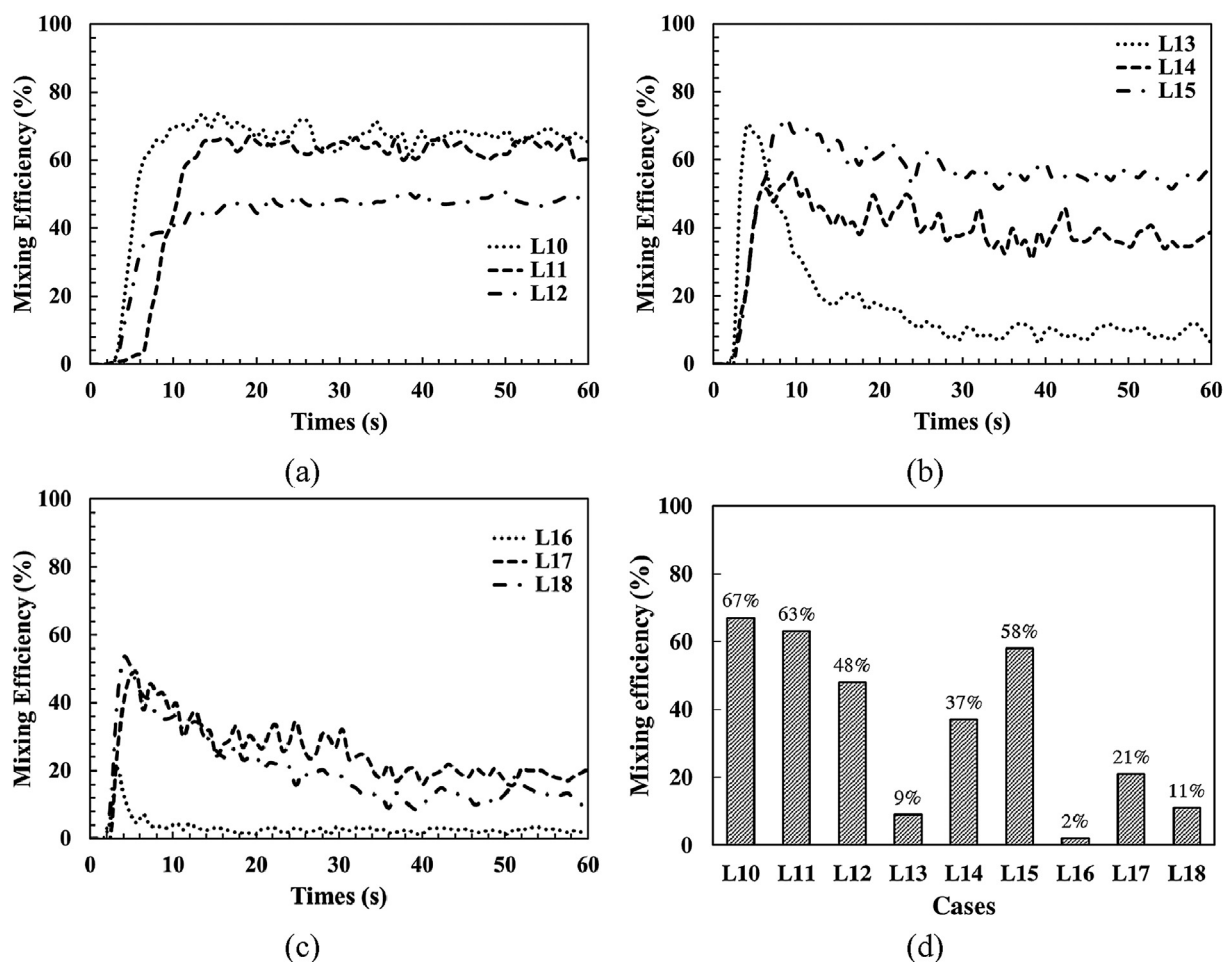


Fig. 8 CFD simulation of mixing efficiencies at lower specific gravity at rotation speeds of 200 rpm for the Cases L10 to L18, (a) Cases L10 to L12, (b) Cases L13 to L15, (c) Cases L16 to L18, and (d) Mixing efficiencies compared for the Cases L10 to L18.

tank, after the mixing becomes steady, as shown in Figs. 2q and 3q. This is because the high clearance from the top of liquid surface to the upper impeller (CV). Case L18 similarly presents low mixing efficiency in the short wide tank. This case has the largest impellers with 6 blades. Visual inspection shows extremely turbulent flow without vortex formation. However, the mixing efficiency is too low because it is the shortest tank and at high rotating speed, which causes spillage and loss of some particles, as shown in Figs. 2r and 3r.

The summary of mixing efficiencies for Cases L10 to L18 at lower and higher specific gravities are shown in Figs. 8d and 9d, respectively. Cases L10, L11, and L15 present the best mixing efficiency, more than 50%, at 200 RPM. In these cases, the rotational speed significantly improves the mixing efficiency, especially when comparing cases L10 to L12 with cases L1 to L3, which have the smallest impellers in this study. In general, if the tank geometry cannot be changed, the easiest way to improve mixing efficiency is increasing the rotational speed. However, increasing rotational speed is not always good for improving mixing efficiency, because it has a limit. For example, in cases L16 to L18, these cases have the largest impellers that should provide good mixing, but the results show low mixing efficiency due to water spillage. This is because large

impellers will generate extremely high flow at high rotational speed.

5.3.3. Effect of mixer dimension at high rotation speed (Cases L19 to L27)

Fig. 2s- α and 3s- α present the CFD simulation with particle dispersion and mixing efficiency of Cases L19 to L27. The mixing efficiency profiles of lower and higher specific gravities are shown in Figs. 10 and 11, respectively. These cases have a rotational speed of 300 RPM. Figs. 10a and 11a give mixing efficiency profiles of cases L19 to L21, which have the smallest impeller diameter. These cases have a mixing efficiency of 75%, 58%, and 60% at low specific gravity and 76%, 52%, and 68% at higher specific gravity. The overall results show that these cases have uniform particle dispersion inside the tank with a steady mixing efficiency profile. Case L19 has 6 blades and a tall narrow tank with high impeller-impeller clearance (S). This case yields good mixing efficiency, about 75%, for both specific gravities, which is the highest mixing efficiency in the 300 RPM set. Although there is a high distance between the upper impeller and the top of liquid surface (CV), there is no vortex formation at high rotational speed, as shown in Fig. 2s and 3s. Case L20 has 8 blades and is a

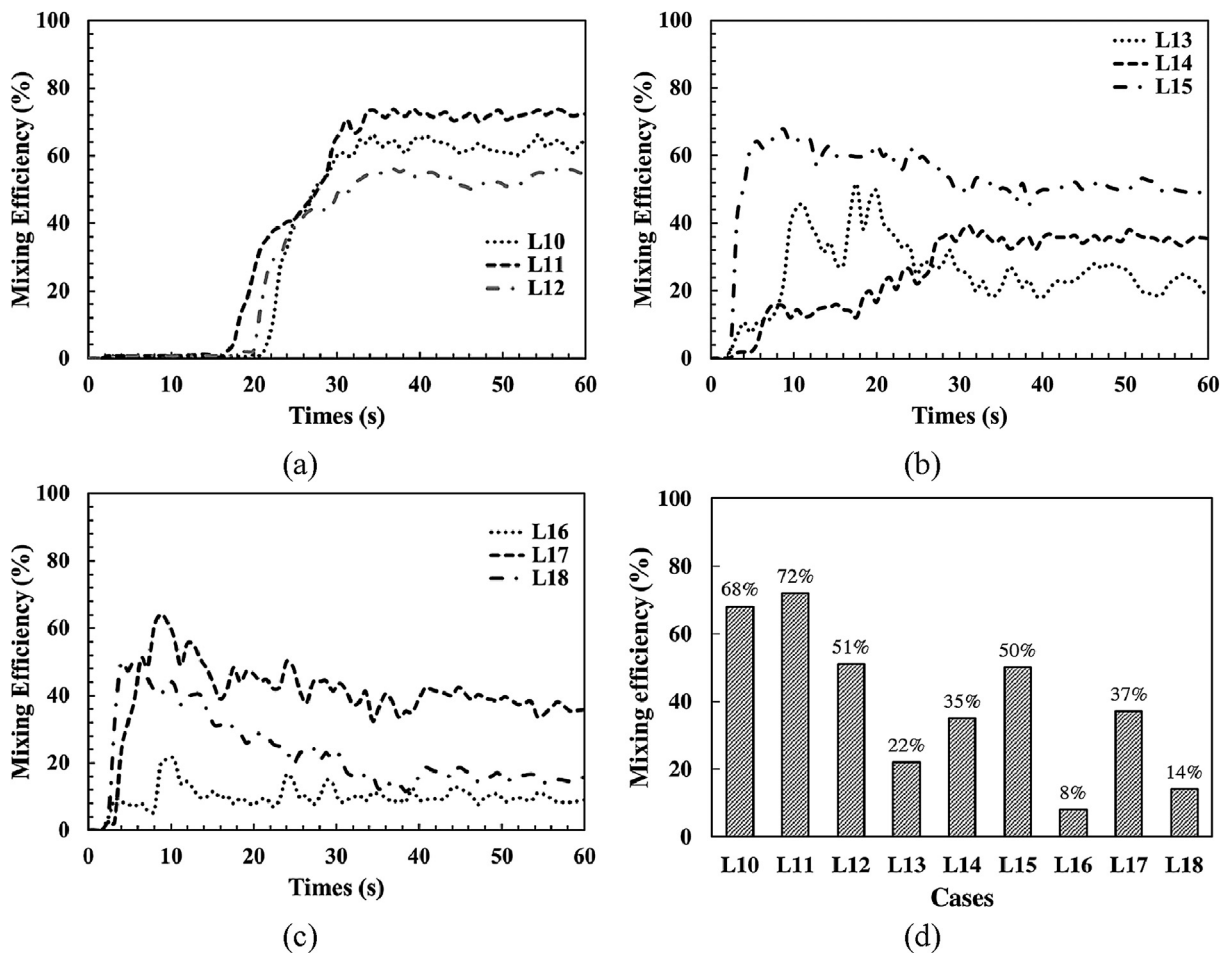


Fig. 9 CFD simulation of mixing efficiencies at higher specific gravity at rotation speeds of 200 rpm for the Cases L10 to L18, (a) Cases L10 to L12, (b) Cases L13 to L15, (c) Cases L16 to L18, and (d) Mixing efficiencies compared for the Cases L10 to L18.

short, medium width tank. Visual inspection reveals a small vortex on the top of liquid surface because the impeller is installed too high (low CV distance), as shown in Fig. 2t and 3t. This case has low mixing efficiency and low particle dispersion in the top of the liquid, which is in the vortex zone. Case L21 has 4 blades and is a large tank with a mixing efficiency of about 60% for both specific gravities. This case has low mixing efficiency because the D/T ratio seems to be low, even if the impeller is installed at a reasonable clearance. Again, this shows that the D/T ratio is an important parameter in the mixer design.

Cases L22 to L24 have an impeller diameter (D) of 150 mm, low impeller-impeller clearance ($S = 100$ mm), and an impeller-bottom clearance (C) of 125 mm, as shown in Figs. 2v-x and 3v-x. These cases also operate at 300 RPM with the mixing efficiency of 35%, 3%, and 40%, respectively, at lower specific gravity and 39%, 4%, and 48%, respectively, at higher specific gravity. The mixing efficiency profiles of these cases at lower and higher specific gravities are shown in Figs. 10b and 11b, respectively. The overall results of these cases demonstrate that the mixer has the highest mixing efficiency at around 5 s and drops significantly approaching steady state. This is because a vortex forms after 10 s, and the resulting bulk flow causes poor mixing thereafter. Case L22 has mixing efficiency of about 35% for both specific gravities. This case has

the same tank size as Case L19, but Case L22 has larger impeller diameter, which might be thought to give higher mixing efficiency. However, Case L22 has lower mixing efficiency than Case L19 because low impeller clearances (S and C) and vortex formation. Case L23 shows extremely turbulent flow in a short medium-wide tank, as seen in Figs. 2w and 3w. This case shows a maximum in mixing efficiency at 45% which then diminishes toward the steady state value of 4%, once again due to the vortex formation in the tank. Case L24 has 4 blades in the large tank with a mixing efficiency of about 40% for both of specific gravities. The result shows a modest vortex on the top of liquid surface. From these results, the deleterious effects of vortex formation are clearly seen. The next cases are the largest impeller with the highest rotation speed for which vortices should be even more problematic.

The mixer cases L25 to L27 are shown in Figs. 2y- α and 3y- α . These cases have the largest impellers and operate at 300 RPM. The mixing profiles of lower and higher specific gravities are shown in Figs. 10c and 11c, respectively. The mixing efficiency for all cases rises rapidly, then slowly decreases, and reach steady state values lower than 10%. All of these cases present a deep vortex formation on the liquid surface that adversely affects the mixer performance. The mixing efficiency of these cases cannot be precisely evaluated due of the deep vortex, extremely turbulent flow, and air bubbles inside the

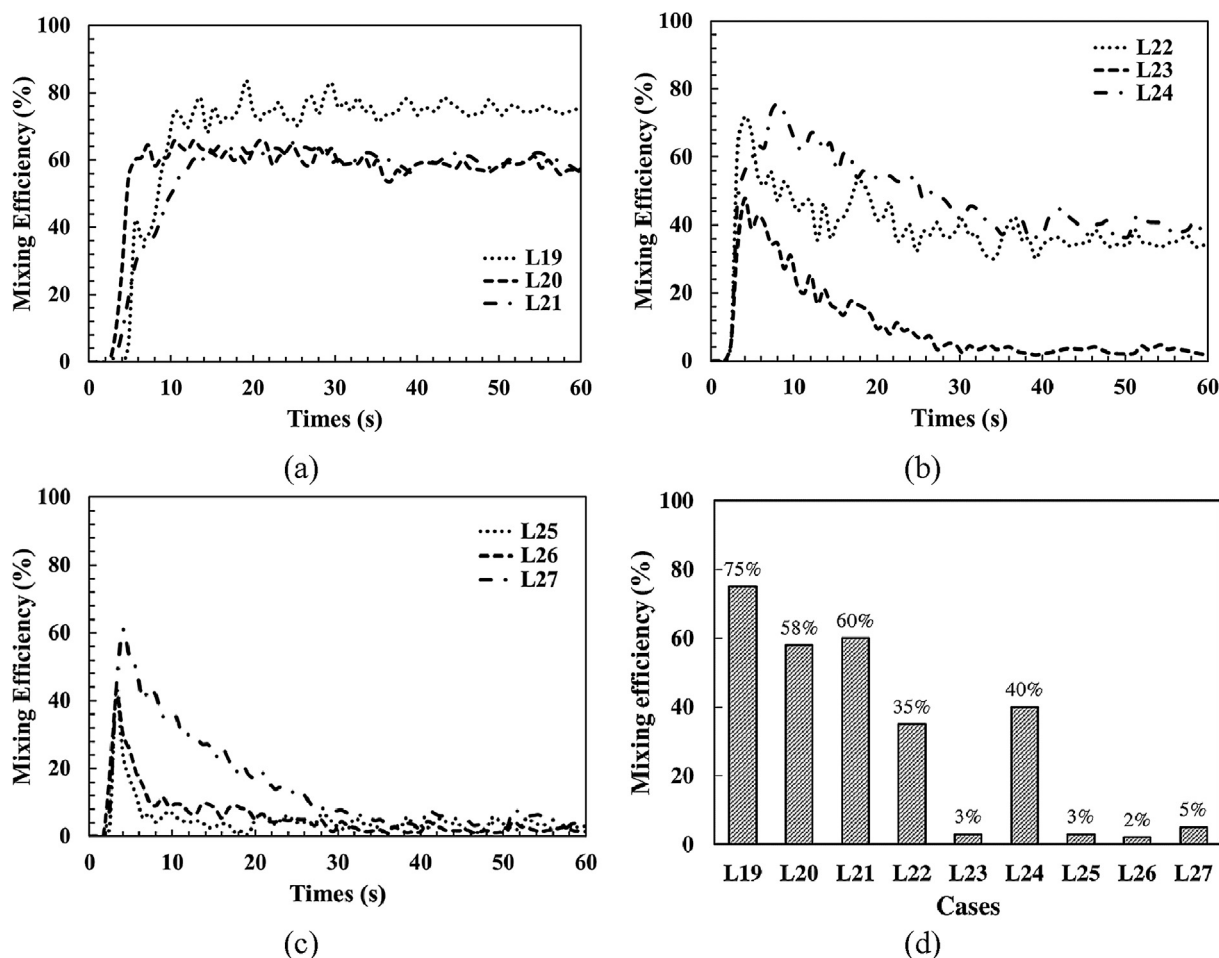


Fig. 10 CFD simulation of mixing efficiencies at lower specific gravity at rotation speeds of 300 rpm for the Cases L19 to L27, (a) Cases L19 to L21, (b) Cases L22 to L24, (c) Cases L25 to L27, and (d) Mixing efficiencies compared for the Cases L19 to L27.

tank, which interfere with image processing. Experimentally, the air bubbles can be eliminated by ensure that the upper impeller is sufficiently far below the water surface.

The overall mixing efficiency of cases L19 to L27 are shown in Figs. 10d and 11d. Cases L19 to L21 give the best mixing efficiency in the 300 RPM group. The results show that the small impeller has more uniform particle dispersion than larger impeller at high rotation speed. Nevertheless, larger impellers can reduce blend time at the same tank size. This is because larger impellers will provide more turbulence and a higher pumping rate. However, there are several disadvantages of the large size. These disadvantages include high rotation speed, a high D/T ratio, and a high CV distance, all of which cause vortex formation, liquid/particles splashing, and air bubbles.

5.4. Signal-to-noise ratio

In any DOE methods (e.g., Taguchi method), the signal-to-noise (S/N) ratio is the indicator used to identify control factors and measure how response varies relative to the target value. There are three basics S/N ratio: “smaller is better,” “larger is better,” and “normal is better,” that can be chosen for the purpose of design. For examples, “smaller is better” is used to minimize the response and the occurrences of some

undesirable product characteristics, and “larger is better” is used to maximize the response. The main goal of using the DOE in this work is to maximize the mixing efficiency with low torque. Therefore, “larger is better” is the S/N ratio that was selected to identify the control factors and define the optimize design of the mixing tank. The “larger is better” S/N ratio is defined as:

$$S/N = -10 \log \left(\frac{\sum \frac{1}{Y^2}}{n} \right) \quad (17)$$

where Y is the response from the system or the mixing efficiency in this study, and n is the number of observations on the particular product. In order to identify the required torque to achieve the degree of mixing suspension, the “smaller is better” is used to investigate the control factors that result in low required torque in the system. The “smaller is better” S/N ratio is defined as:

$$S/N = -10 \log \left(\frac{\sum Y^2}{n} \right) \quad (18)$$

The S/N ratios with “lower is better” is used to capture the required torque to achieve the degree of mixing in the system, as shown in Fig. 12a. The result shows that the most significant control factors are the impeller-impeller diameter (D) and rota-

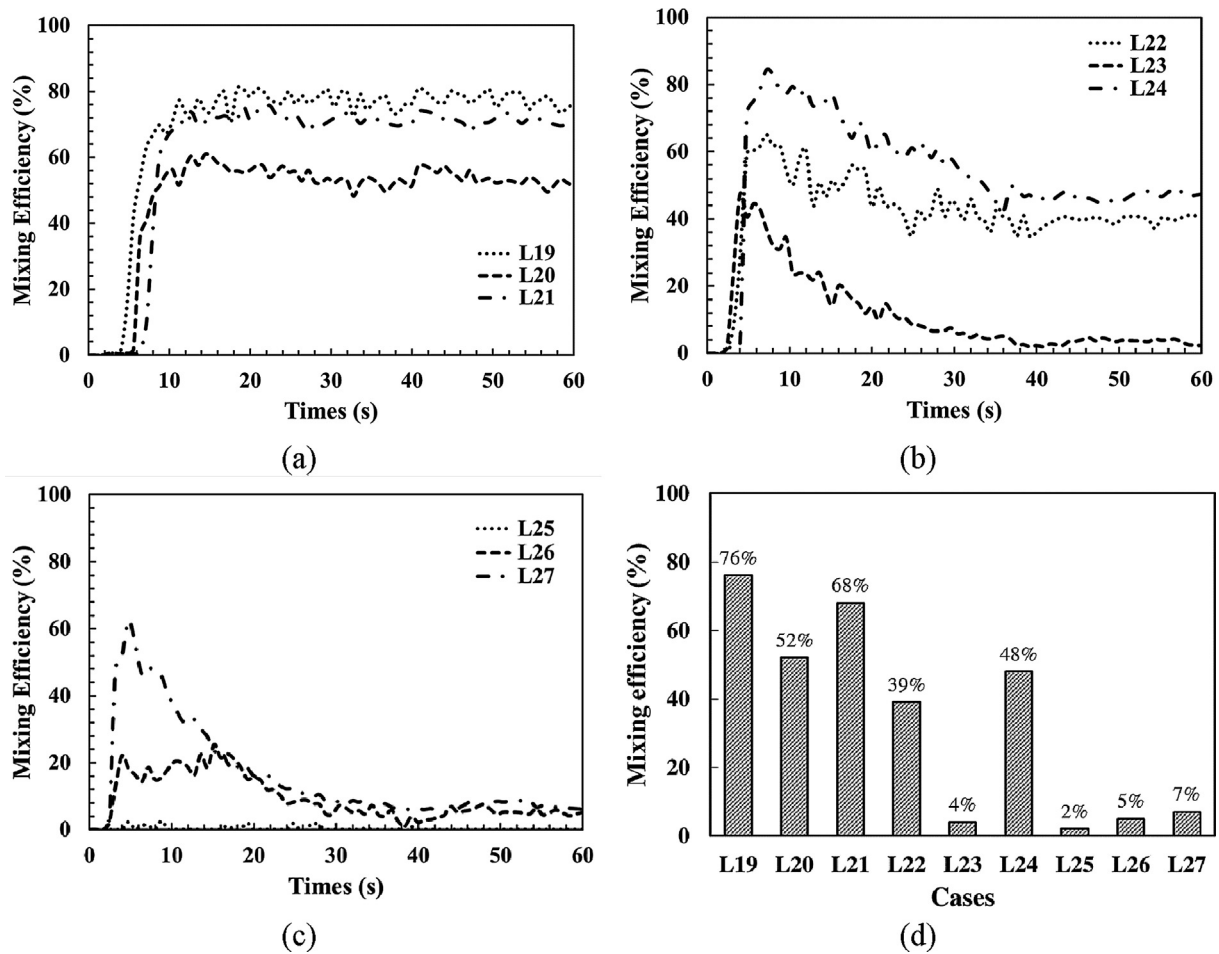


Fig. 11 CFD simulation of mixing efficiencies at higher specific gravity at rotation speeds of 300 rpm for the Cases L19 to L27, (a) Cases L19 to L21, (b) Cases L22 to L24, (c) Cases L25 to L27, and (d) Mixing efficiencies compared for the Cases L19 to L27.

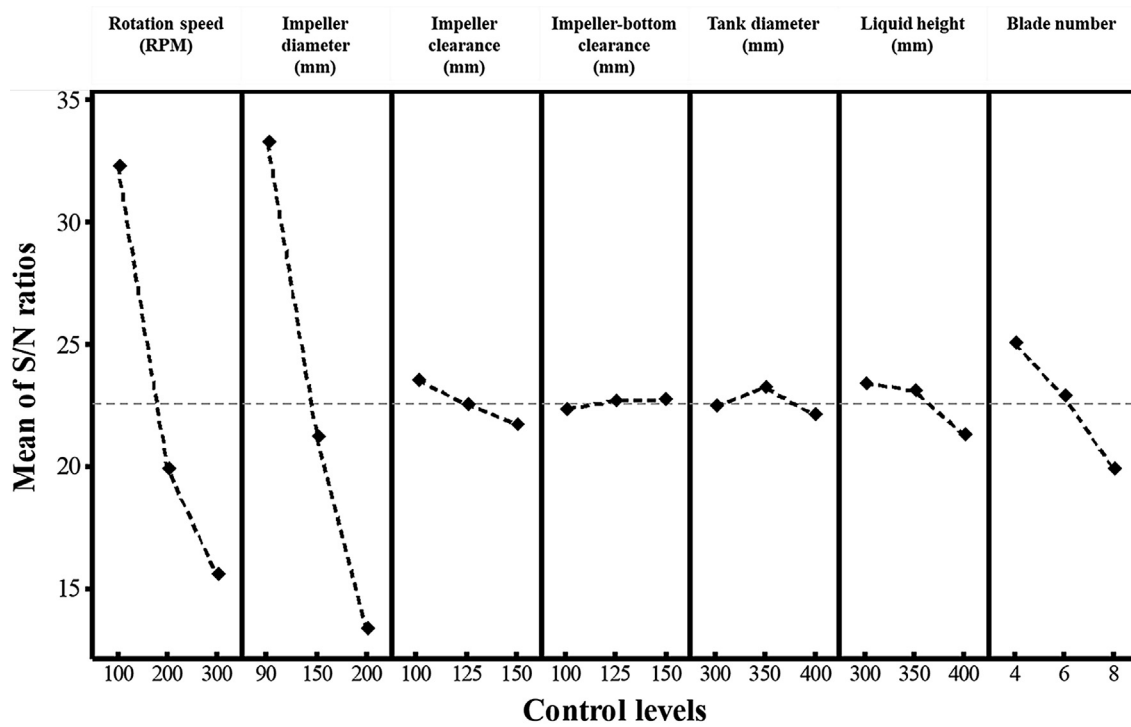
tion speed (*RPM*). Interestingly, the impeller-bottom clearance (*C*), liquid height (*H*), and tank diameter (*T*) show little impact on the required torque in the mixing system. Fig. 12b summarizes the mean of signal-to-noise ratios used in this study. These charts plot the *S/N* ratios versus the levels of each control factor. The *S/N* ratios include all of the response *Y* (mixing efficiency) for both specific gravities. From these charts, the most influential control factors are the rotation speed, blade diameter, impeller-impeller clearance (*S*) and impeller-bottom clearance (*C*). These show that the clearance between both impellers of contra-rotating impellers needs to be carefully adjusted. The result shows that the liquid height (*H*) and tank diameter (*T*) have less impact on the mixing efficiency. However, the system will have low mixing efficiency if the improper impellers are installed. The above results also suggest that appropriate clearance of impellers can prevent vortex formation and water spillage.

5.5. Design guidelines for pitched-blade contra-rotating impellers with inward opposing flow

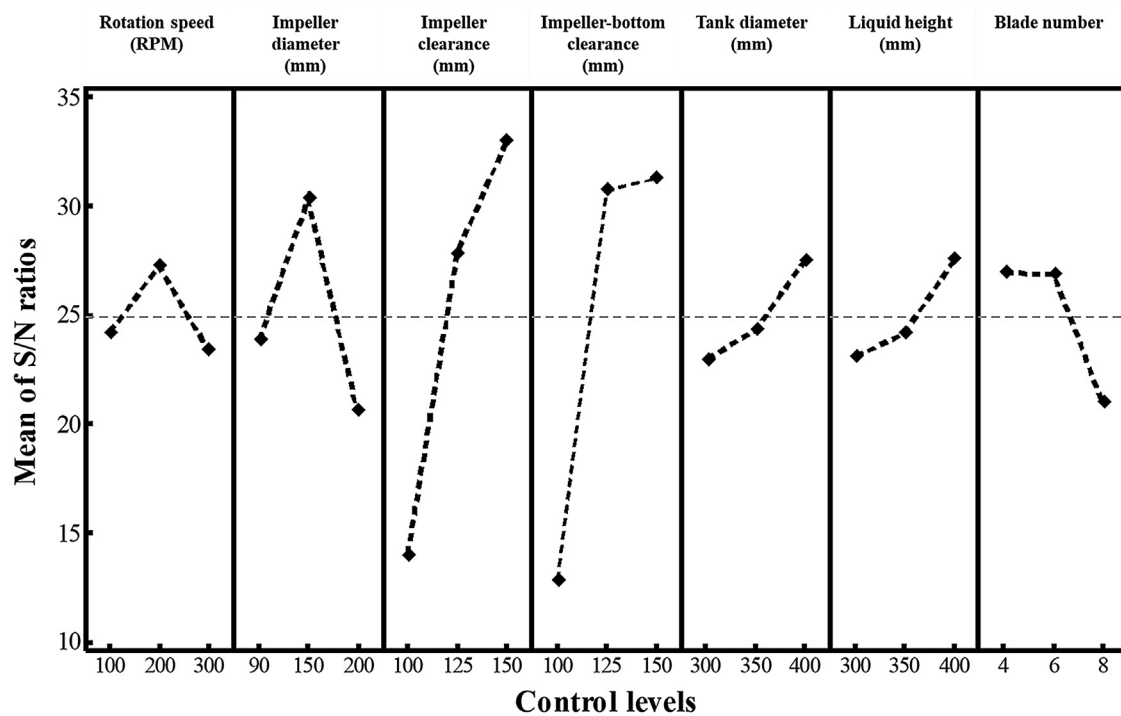
In a laboratory or pilot scale tank, the first parameter to adjust is the impeller rotation speed, which can change the pumping capacity, blend time, mass transfer, and shear rates. Uniform

particles dispersion is required for solid-catalyzed reaction and suspension polymerization, where improper design may lead to poor mixing efficiency. From the results in Fig. 4a, our criteria is that if the mixing efficiency is more than 60% and the torque is lower than 0.1 N.m, the design will be optimized. The result shows that Cases L4, L5, L6, L8, L10, L11, L19, and L21 have fallen under that optimized criteria. Further, case L4 provides the highest mixing efficiency with the lowest torque. Therefore, Case L4 will be the best design from this study. Based on the *S/N* ratio analysis from Fig. 12 and considering design parameters to achieve high mixing efficiency with low torque, the suggested range of design parameters are shown in Table 4. The recommended pilot scale mixer design for solid-liquid mixing with inward flow contra-rotating, baffle-free impeller is shown in the following lists:

- A cylindrical tank with a round bottom, induces flow patterns responsible for lifting solid up from the bottom and eliminates the dead zone in bottom corners of a cylindrical tank with a flat bottom.
- The aspect ratio of the contra-mixed tank is optimized with a ratio of liquid height to tank diameter (*H/T*) in the range of $1 < H/T < 1.35$.
- The ratio of the impeller to tank diameter (*D/T*) should be in the range of $0.35 < D/T < 0.50$.



(a)



(b)

Fig. 12 (a) Mean of signal to noise (S/N) ratio with “Smaller is better” for optimal torque require to achieve mixing efficiency and (b) Mean of signal to noise (S/N) ratio with “Larger is better” for optimal mixing efficiency.

Table 4 Suggestion range of design parameters to achieve high mixing efficiency with low torque.

| Rotation speed (RPM) | Impeller diameter (mm) | Impellers clearance (mm) | Impeller-bottom clearance (mm) | Tank diameter (mm) | Liquid height (mm) | Blade Number (n) |
|----------------------|------------------------|--------------------------|--------------------------------|--------------------|--------------------|------------------|
| 100 | 90 | 100 | 125 | low impact | low impact | 4 |
| to | to | to | to | | | to |
| 200 | 150 | 150 | 150 | | | 6 |

- The ratio of the liquid coverage above upper impeller to the liquid height (CV/H) should be in the range of $0.20 < CV/H < 0.30$ to prevent vortex formation at high rotation speed.
- Baffles are not required for solids suspension operations for particles that are heavier or lighter than the liquid.

The design guidelines for pitched-blade contra-rotating, baffle-free impeller with the inward opposing flow was found in the following configuration: $\frac{H}{T} \approx 1$, $\frac{D}{T} \approx 0.38$, $\frac{C}{T} \approx 0.36$, $\frac{S}{D} \approx 1.10$, $\frac{C}{H} \approx 0.37$, and $\frac{CV}{H} \approx 0.25$.

6. Conclusion

Design of experiment (Taguchi method) yields an outstanding outcome by optimizing the process design parameters and reducing the number of experiments through orthogonal arrays. The S/N ratios can identify the impact of design parameters on the mixing efficiency and provide the optimum design of mixer configuration. CFD simulation in parallel with DOE can optimize processes and increase the quality of products such as the efficiency of a mixing tank. Because conventional experimental design techniques, such as a full factorial DOE, tend to have drawbacks and limitations, this DOE approach shows promise as an attractive optimization tool for engineers and scientists.

Mixing design optimization in a pitched-blade contra-rotating, baffle-free impeller with inward flow can be dependably demonstrated via CFD simulation combined with design of experiments, image analysis, and S/N ratios. The design-of-experiments method provides fast-design guidelines and an optimum mixer design while the S/N ratios can identify the impact of design parameters on the mixing efficiency. CFD simulation can yield fundamental understanding and can be used to better understand solid-liquid mixing characteristics. In this study, the most influential control factors that affect the mixing efficiency are the impeller-impeller clearance (S) and impeller-bottom clearance (C). The effect of torque on mixing efficiency must also be considered to find the optimal design of the mixing tank. Based on the overall results, the optimal design for both specific gravities is Case L4, which has high mixing efficiency at low torque. Further study of scale-up factors (i.e., dimensionless ratio of design parameters) as well as the other flow configurations in contra-rotating impellers such as outward, down-down, and up-up are likely to be fruitful.

Declaration of Competing Interest

The authors declare the following financial interests/personal relationships which may be considered as potential

competing interests: [The 3rd author (JAR) works for Perfect Mixing LLC. Other authors have no conflict of interest.]

Acknowledgement

The authors would like to thank Perfect Mixing LLC for providing the experimental equipment. The authors also would like to acknowledge Dassault Systèmes Simulia S.L.U. for providing the XFlow software. Finally, the authors would like to recognize Mr. Drew Pereira, Mr. Michael Brizes, and Mr. Mitchell Sepe for proofreading our manuscript. Finally, the authors would like to acknowledge the collaboration agreement between University of South Carolina and Chiang Mai University.

Appendix A. Supplementary material

Supplementary data to this article can be found online at <https://doi.org/10.1016/j.aej.2021.02.045>.

References

- [1] E.L. Paul, V. Atiemo-Obeng, S.M. Kresta, *Handbook of Industrial Mixing: Science and Practice*, John Wiley & Sons Inc, Hoboken, NJ, 2004.
- [2] J.R. Regalbuto, J.A. Regalbuto, Method and Apparatus for Improved Mixing of Solid, Liquid, or Gaseous Materials and Combinations Thereof. US Patent. 20140078858 :A1 (2014).
- [3] P. Satjaritanun, E. Bringley, J.R. Regalbuto, J.A. Regalbuto, J. Register, J.W. Weidner, Y. Khunatorn, S. Shimpalee, Experimental and computational investigation of mixing with contra-rotating, baffle-free impellers, *Chem. Eng. Res. Des.* 130 (2018) 63–77.
- [4] Q. Wang, D. Meng, A study of the matching of impellers and motors for contra-rotating fan based on electromagnetic-fluid coupling analysis, *Adv. Mech. Eng.* 8 (2016) 1–11.
- [5] K.J. Paik, S. Hwang, J. Jung, T. Lee, Y.Y. Lee, H. Ahn, S.H. Van, Investigation on the wake evolution of contra-rotating propeller using RANS computation and SPIV measurement, *Int. J. Nav. Archit. Ocean Eng.* 7 (2015) 595–609.
- [6] K.S. Min, B.J. Chang, H.W. Seo, Study on the Contra-Rotating Propeller system design and full-scale performance prediction method, *Int. J. Nav. Archit. Ocean Eng.* 1 (2009) 29–38.
- [7] S. Gaggeroa, J. Gonzalez-Adalidb, M.P. Sobrinob, Design and analysis of a new generation of CLT propellers, *Appl. Ocean Res.* 59 (2016) 424–450.
- [8] D. Grassi, S. Brizzolara, M. Viviani, L. Savio, S. Caviglia, Design and analysis of counter-rotating propellers-comparison of numerical and experimental results, *J. Hydrodyn. (B)* 22 (2010) 570–576.
- [9] F. Çelik, M. Güner, Energy saving device of stator for marine propellers, *Ocean Eng.* 34 (2007) 850–855.

- [10] I. Fořt, J. Hájek, V. Machoň, Energetic efficiency of two impellers on the same shaft in a cylindrical baffled vessel of high height/diameter ratio, *Coll. Czech. Chem. Commun.* 54 (1989) 2345–2356.
- [11] I. Fořt, V. Machoň, J. Hájek, E. Fialová, Liquid Circulation in a cylindrical baffled vessel of high height/diameter ratio with two impellers on the same shaft, *Coll. Czech. Chem. Commun.* 52 (1987) 2640–2653.
- [12] J. Antony, *Design of Experiments for Engineers and Scientists*, Elsevier, Massachusetts, 2014.
- [13] A.J. Keane, Wing optimization using design of experiment, response surface, and data fusion methods, *JA.* 40 (2003) 741–750.
- [14] Y. Guo, Investigating the effect of chromatographic conditions on retention of organic acids in hydrophilic interaction chromatography using a design of experiment, *Chromatographia* 66 (2007) 223–229.
- [15] G. Blondet, J.L. Duigou, N. Boudaoud, B. Eynard, An ontology for numerical design of experiments processes, *Comput. Ind.* 94 (2018) 26–40.
- [16] G. Taguchi, S. Chowdhury, Y. Wu, *Taguchi's Quality Engineering Handbook*, John Wiley & Sons Inc., Hoboken, NJ, 2005.
- [17] G. Taguchi, R. Jugulum, S. Taguchi, *Computer-Based Robust Engineering: Essential for DFSS*, ASQ Quality Press, Milwaukee, WI, 2004.
- [18] A. Joshaghani, A.A. Ramezani pour, O. Ataei, A. Golroo, Optimizing pervious concrete pavement mixture design by using the Taguchi method, *Constr. Build. Mater.* 101 (2015) 317–325.
- [19] M. Azin, R. Moravej, D. Zareh, Production of xylanase by *Trichoderma longibrachiatum* on a mixture of wheat bran and wheat straw: Optimization of culture condition by Taguchi method, *Enzyme. Microb. Technol.* 40 (2007) 801–805.
- [20] W.H. Yang, Y.S. Tarn, Design optimization of cutting parameters for turning operations based on the Taguchi method, *J. Mater. Proc. Technol.* 84 (1998) 122–129.
- [21] A. Mohammad-Ez-Abadi, M. Sadi, M. Farzaneh-Gord, M. Hossein-Ahmadi, R. Kumar, K.-W. Chau, A numerical and experimental study on the energy efficiency of a regenerative Heat and Mass Exchanger utilizing the counter-flow Maisotsenko cycle, *Eng. Appl. Comput. Fluid Mech.* 14 (2020) 1–12.
- [22] E. Akbarian, B. Najafi, M. Jafari, S. Faizollahzadeh-Ardabili, S. Shamshirband, K.-W. Chau, Experimental and computational fluid dynamics-based numerical simulation of using natural gas in a dual-fueled diesel engine, *Eng. Appl. Comput. Fluid Mech.* 12 (2018) 517–534.
- [23] M. Ramezanizadeh, M. Alhuyi-Nazari, M. Hossein-Ahmadi, K.-W. Chau, Experimental and numerical analysis of a nanofluidic thermosyphon heat exchanger, *Eng. Appl. Comput. Fluid Mech.* 13 (2019) 40–47.
- [24] P. Satjaritanun, Y. Khunatorn, N. Vorayos, S. Shimpalee, E. Bringley, Numerical analysis of the mixing characteristic for napier grass in the continuous stirring tank reactor for biogas production, *Biomass Bioenerg.* 86 (2016) 53–64.
- [25] I. Ayranci, S.M. Kresta, J.J. Derksen, Experiments and simulations on bidisperse solids suspension in a mixing tank, *Chem. Eng. Technol.* 36 (2013) 1957–1967.
- [26] H. Zbib, M. Ebrahimi, F. Ein-Mozaffari, A. Lohi, Comprehensive analysis of fluid-particle and particle-particle interactions in a liquid-solid fluidized bed via CFD-DEM coupling and tomography, *Powder Technol.* 340 (2018) 116–130.
- [27] A. Yaraghi, M. Ebrahimi, F. Ein-Mozaffari, A. Lohi, Mixing assessment of non-cohesive particles in a paddle mixer through experiments and discrete element method (DEM), *Adv Powder Technol.* 29 (2018) 2693–2706.
- [28] S.D. Bolboacă, L. Jäntschi, *Design of Experiments: Useful Orthogonal Arrays for Number of Experiments from 4 to 16*, *Entropy.* 9 (2007) 198–232.
- [29] A. Kukukova, J. Aubin, S.M. Kresta, A new definition of mixing and segregation: Three dimensions of a key process variable, *Chem. Eng. Res. Des.* 87 (2009) 633–647.
- [30] A. Kukukova, J. Aubin, S.M. Kresta, Measuring the scale of segregation in mixing data, *Can. J. Chem. Eng.* 89 (2011) 1122–1138.
- [31] P.M.C. Lacey, Developments in the theory of particle mixing, *J. Appl. Chem.* 4 (1954) 257–268.
- [32] P.M.C. Lacey, F.S.M.A. Mirza, A study of the structure of imperfect mixtures of particles. Part I. Experimental technique, *Powder Technol.* 14 (1976) 17–24.
- [33] P.M.C. Lacey, F.S.M.A. Mirza, A study of the structure of imperfect mixtures of particles. Part II. Experimental technique, *Powder Technol.* 14 (1976) 25–33.
- [34] P. Larosa, F.S. Manning, Intensity of segregation as a measure of incomplete mixing, *Can. J. Chem. Eng.* 42 (1964) 65–68.
- [35] N. Harnby, A comparison of the performance of industrial solids mixers using segregating materials, *Powder Technol.* 1 (1967) 94–102.
- [36] R. Dlugi, M. Berger, M. Zelger, A. Hofzumahaus, F. Rohrer, F. Holland, K. Lu, G. Kramm, The balances of mixing ratios and segregation intensity: a case study from the field (ECHO 2003), *Atmos. Chem. Phys.* 14 (2014) 10333–10362.
- [37] U. Frisch, B. Hasslacher, Y. Pomeau, Lattice-gas automata for the navier-stokes equation, *Phys. Rev. Lett.* 56 (1986) 1505–1508.
- [38] G.R. McNamara, G. Zanetti, Use of the Boltzmann equation to simulate lattice-gas automata, *Phys. Rev. Lett.* 61 (1988) 2332–2335.
- [39] S. Chen, G.D. Doolen, Lattice Boltzmann method for fluid flows, *Annu. Rev. Fluid Mech.* 30 (1998) 329–364.
- [40] X. Shan, H. Chen, A general multiple-relaxation-time Boltzmann collision model, *Int. J. Mod. Phys. C.* 18 (2007) 635–643.
- [41] D. d'Humieres, Multiple relaxation time Lattice Boltzmann models in three dimensions, *Phil. Trans. R. Soc. Lond. A.* 360 (2002) 437–451.
- [42] K. Premnath, S. Banerjee, On the three-dimensional central moment Lattice Boltzmann method, *J. Stat. Phys.* 143 (2012) 747–761.
- [43] P. Satjaritanun, J.W. Weidner, S. Hirano, Z. Lu, Y. Khunatorn, S. Ogawa, S.E. Litster, A.D. Shum, I.V. Zenyuk, S. Shimpalee, Micro-scale analysis of LiquidWater breakthrough inside gas diffusion layer for PEMFC using X-ray computed tomography and lattice Boltzmann method, *J. Electrochem. Soc.* 164 (2017) E3359–E3371.
- [44] M. Mezhericher, T. Brosh, A. Levy, Modeling of particle pneumatic conveying using DEM and DPM method, *Particul. Sci. Technol.* 29 (2011) 197–208.
- [45] W. McCabe, J. Smith, P. Harriott, *Unit Operations of Chemical Engineering*, McGraw Hill Chemical Engineering Series, NY, 2004.
- [46] D. Chapple, S.M. Kresta, A.E. Wall, A. Afacan, The effect of impeller and tank geometry on power number for a pitched blade turbine, *Trans. IChemE.* 80 (2002) 364–372.
- [47] X. Wang, K. Walters, Computational analysis of marine-propeller performance using transition-sensitive turbulence modeling, *Trans. ASME.* 134 (2012) 0711071–07110710.
- [48] Dassault Systèmes Simulia S.L.U. XFlow, <https://www.3ds.com/products-services/simulia/products/xflow/>. (2020). Accessed 21 May 2020.
- [49] I.V. Shevchuk, *Modelling of Convective Heat and Mass Transfer in Rotating Flows*, Springer International Publishing, Switzerland, 2016.

- [50] W. Siddique, L. El-Gabry, I.V. Shevchuk, T.H. Fransson, Validation and analysis of numerical results for a two-pass trapezoidal channel with different cooling configurations of trailing edge, *J. Turbomach.* 135 (2013) 011027–11031.
- [51] W. Siddique, I.V. Shevchuk, L. El-Gabry, N.B. Hushmandi, T. H. Fransson, On flow structure, heat transfer and pressure drop in varying aspect ratio two-pass rectangular channel with ribs at 45°, *Heat Mass Transfer.* 49 (2013) 679–694.